EES Catalysis

PAPER

View Article Online
View Journal

Cite this: DOI: 10.1039/d5ey00328h

Dynamic structural evolution of 2D/3D MoS_2@Ni heterostructure supported on SBA-15 during CO_2 RWGS reaction

Oumayma Liaaychi,[ab] Pascal Blanchard,[b] Maya Marinova,[c] Carole Lamonier,[b] Jean-Philippe Dacquin,*[b] Sébastien Royer *[d] and Said Laassiri*[a]

Received 14th November 2025,
Accepted 28th January 2026

DOI: 10.1039/d5ey00328h

rsc.li/eescatalysis

Two-dimensional (2D) layered materials have attracted significant interest for catalytic applications due to tuneable electronic properties, and a high density of edge-active sites associated to a high proportion of reactant-accessible active sites. In this work, we report the synthesis of 2D/3D MoS_2@Ni/SBA-15 heterostructure *via* thermal *in situ* gas-phase sulfidation of MoO_3@NiO/SBA-15 precursor, aimed at promoting reverse water–gas shift (RWGS) reaction. Catalytic tests, conducted over a wide temperature range (200–800 °C) revealed that the MoS_2@Ni/SBA-15 catalyst significantly outperforms its oxidic counterpart in terms of product selectivity, while both catalysts exhibit high CO_2 conversion. Notably, the sulfided heterostructure achieves complete suppression of CH_4 formation and maintains 100% selectivity towards CO across the entire temperature range studied. In contrast, MoO_3@NiO/SBA-15 favours methanation at low temperatures and only shifts to CO production at $T > 600$ °C. At 500 °C, a CO_2 conversion of 33.3% is achieved on MoS_2@Ni/SBA-15 with exclusive CO selectivity, surpassing most state-of-the-art transition metal-based catalysts operating at similar conditions. Moreover, long-term stability tests at 800 °C, over 100 h, confirmed its remarkable stability, maintaining high CO_2 conversion (>75%) and full CO selectivity without any visible deactivation. These results demonstrate the strong potential of engineered 2D/3D MoS_2-based heterostructures as efficient, robust, and non-noble metal catalysts for sustainable CO_2 valorisation.

Broader context

Mitigating anthropogenic CO_2 emissions requires not only efficient capture technologies but also valorization processes that enable a selective conversion of CO_2 into chemical intermediates. The reverse water gas shift (RWGS) reaction is particularly attractive, as it allows the transformation of CO_2 into CO, a key feedstock for the synthesis of clean fuels and chemicals when coupled with renewable hydrogen. However, achieving high activity with full selectivity to CO remains challenging. The development of noble metal free catalysts is of particular interest for this reaction. Here Ni–Mo_2C/SBA-15 catalyst is selective to the RWGS reaction. *In situ* formation of molybdenum carbide modifies the electronic and interfacial properties of nickel, suppressing undesired methane formation while promoting CO production. This metal–carbide synergy allows control over the reaction pathway under hydrogen-rich conditions relevant to power-to-X applications. Fully selective and stable Ni–Mo_2C/SBA-15 RWGS catalyst provides a robust and scalable route to CO production, facilitating the integration of CO_2 valorization into industrial processes. By combining non-noble metals, high selectivity and stability, these catalysts can contribute to the development of economically viable clean technologies for carbon recycling and industrial decarbonization.

Introduction

Over the past decades, two dimensional (2D) layered materials have emerged as versatile materials for catalysis due to their atomically thin structures, large surface areas, and highly tunable electronic properties.[1,2] Unlike, their 3D (bulk) counterparts, 2D systems exhibit unique surface reactivity derived from, abundance of edge sites, quantum confinement effects, and anisotropic charge transport. These features make 2D-based catalysts attractive candidates for applications including hydrogen evolution, CO_2 reduction, hydrodesulfurization, ammonia synthesis, and electrocatalysis.[3–6]

[a] *Chemical & Biochemical Sciences, Green Process Engineering (CBS), Mohammed VI Polytechnic University, UM6P, 43150, Benguerir, Morocco. E-mail: Said.LAASSIRI@um6p.ma*
[b] *Université de Lille, CNRS, ENSCL, Centrale Lille, Université Artois, UMR 8181-UCCS-Unité de Catalyse et de Chimie du Solide, F-59000 Lille, France*
[c] *Université de Lille, CNRS, INRA, Centrale Lille, Université Artois, FR 2638 – IMEC – Institut Michel-Eugène Chevreul, 59000 Lille, France*
[d] *Université du Littoral Côte d'Opale, UCEIV UR 4492, MREI-1, 145 Avenue Maurice Schumann, 59140 Dunkerque, France*

Among 2D materials, MoS_2 has emerged as a promising catalyst for CO_2 activation and conversion due to its tunable electronic structure and defect engineering potential.[7] Traditional transition metal catalysts, such as Cu/ZnO-based catalysts,[8] and Ni-based catalysts,[9] have been extensively investigated for the RWGS reaction; these catalysts have significant limitations, including low thermal stability and reduced activity/selectivity at low operating temperatures.[10,11] In particular, classical Cu-based RWGS catalysts typically require reaction temperatures above 600 °C to reach adequate CO_2 conversion and suppress undesired methane formation. This high-temperature requirement leads to elevated energy consumption that increases the overall process cost and inducing CO_2 emissions associated with heat production, posing challenges for economic and sustainable operation.[12,13] Although recent advances involving Pd, Ru, and Ce-based catalysts have shown improved performance for the RWGS reaction, challenges related to long-term stability and cost-effectiveness still hinder their practical application in large-scale processes.[14–17]

Layered transition metal dichalcogenides (TMDCs) such as MoS_2 offer an attractive alternative due to their two-dimensional structure, high density of exposed edge sites, and capacity for electronic modulation through doping or heterostructure formation.[7,18] However, the practical application of 2D MoS_2 in thermal catalysis remains limited by its tendency to restacking and agglomeration under reaction conditions.[19,20] This structural collapse reduces the accessible active surface area and limits mass transport, ultimately hindering their performance in heterogeneous catalysis.[19] One effective approach to overcome this limitation involves coupling 2D MoS_2 with three-dimensional (3D) architecture.[21,22] In such 2D/3D configuration, nanosheet aggregation is suppressed while the dispersion of MoS_2 is improved.[21,22] Furthermore, interfacial effects may arise such as interfacial strain, electron transfer, and charge redistribution which can lead to important changes in catalytic activity and selectivity. In particular electron transfer between Ni and Mo plays a crucial role in modulating the catalytic behaviour of Ni–Mo systems, as it directly affects the electronic structure of the active species. In their study, Yang *et al.* provided compelling evidence for strong interaction between Ni and Mo species from XPS analysis.[23] Upon incorporation of Ni ($Ni_1Mo_1/MgAl_2O_4$), the Mo3d peak shifted to a lower binding energy, clearly demonstrating electron transfer from Ni to MoO_x species. This shift in binding energy highlights a strong electronic interaction between the two components, which has been associated with enhanced hydrogen spillover and improved catalytic activity in methyl palmitate hydrogenation. Similar findings by Zhou *et al.* suggested that electronic modification of Ni by Mo could also promote phenol hydrodeoxygenation activity.[24] These observations underline the need for deeper investigation into the electronic interactions and reaction mechanisms of Ni–Mo based catalysts, to fully elucidate their role in catalytic reactions.

In this work, we report a novel approach for the preparation of a 2D/3D MoS_2@Ni/SBA-15 heterostructure for thermo-catalytic CO_2 activation. The 2D/3D MoS_2@Ni/SBA-15 heterostructure was synthesised *via in situ* gas-phase sulfidation of a MoO_3@NiO/SBA-15 oxidic precursor. The catalytic performance was evaluated over a wide temperature range (200–800 °C) and benchmarked against a non-sulfided MoO_3@NiO/SBA-15 catalyst. While the reference catalyst exhibited CH_4 generation at low temperatures and achieved high CO selectivity only at elevated temperatures, the 2D/3D MoS_2@Ni/SBA-15 heterostructure displayed complete suppression of CH_4 and maintained 100% selectivity towards CO across the entire temperature range. Comprehensive characterization reveals that both Mo oxide and MoS_2 precursors undergo controlled *in situ* carburization during the RWGS reaction, leading to the formation of Ni–Mo mixed carbides that profoundly alter the hydrogenation behaviour of Ni and steer selectivity toward CO. This self-activated transformation offers a mild and practical route to carbide formation directly under reaction conditions, avoiding harsh external carburization treatments and preventing re-oxidation issues commonly encountered with pre-synthesized carbides. These findings establish a clear structure–performance relationship linking precursor chemistry, carburization onset, interfacial reconstruction, and catalytic selectivity, and they provide a useful framework for the rational design of highly selective carbide-based RWGS catalysts.

Results and discussion

Structural characteristics of MoS_2@Ni/SBA-15 heterostructure

The 2D/3D MoS_2@Ni/SBA-15 heterostructure was synthesised by gas-phase sulfidation of a MoO_3@NiO/SBA-15 oxidic precursor. The morphological evolution from the oxidic precursor to the 2D/3D heterostructure was investigated by high-angle annular dark-field scanning TEM measurements (HAADF-STEM). As illustrated in Fig. 1a–c, the MoO_3@NiO/SBA-15 oxidic precursor displays a heterogeneous distribution of NiO and MoO_3 particles with no observable 2D layered structures. The majority of Mo oxide particles seems predominantly confined within the micropores of the SBA-15 support, exhibiting a particle size mostly <0.5 nm, indicative of a dispersion at the few-atoms/sub-nanometric scale. In contrast, Ni oxide particles were mainly located within the mesoporous channels of SBA-15, displaying a significantly larger average particle size of approximately 8.4 ± 1.2 nm, as it was already observed by using IWI of transition metal nitrates on mesoporous silica.[25]

After the gas-phase sulfidation step, a significant morphological transformation is observed (Fig. 1d–f). The synthesis method successfully promotes the formation of MoS_2 nanosheets with mono- to few- layers (1–3 layers) with varying lateral dimensions. Low-magnification HAADF-STEM imaging (Fig. 1d–f) clearly reveals the development of a 2D/3D MoS_2@Ni heterostructure, in which ultrathin MoS_2 nanosheets are predominantly anchored onto three-dimensional Ni nanoparticles. However, some individual MoS_2 nanosheets comprising one to three layers are also observed in regions without Ni nanoparticles (Fig. S1).

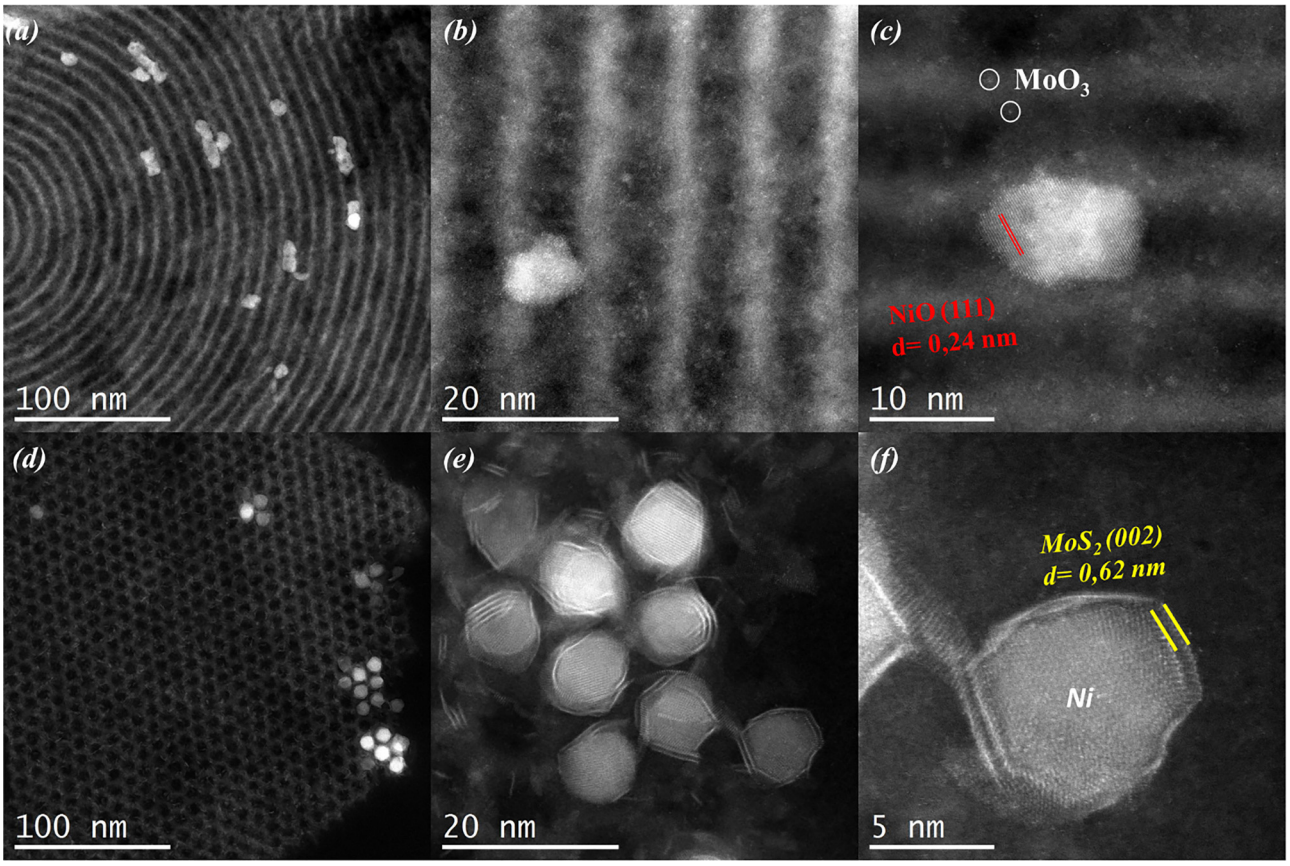

Fig. 1 HAADF-STEM images of (a)–(c) MoO_3@NiO/SBA-15 and (d)–(f) 2D/3D MoS_2@Ni/SBA-15.

To further investigate the elemental distribution, EDS intensity profiles were extracted from the EDS hyperspectral sets. As shown in Fig. 2a–c for MoO_3@NiO/SBA-15 and Fig. 2d–f for 2D/3D MoS_2@Ni/SBA-15, both Mo and Ni are homogeneously distributed in the core region of the silica support.

In MoO_3@NiO/SBA-15, some Mo is located inside silica in area free of Ni (Fig. 2a and b). For both samples, on the Mo–Ni co-located areas, Mo signal spans a wider diameter than that of Ni, indicating Mo surface enrichment. This confirms the formation of a 2D/3D mixed-phase heterostructure, where Mo and Ni are co-located, but Mo is more concentrated near the surface, forming MoS_2-ultrathin layers over a Mo–Ni-rich core after sulfidation.

Additional structural information was obtained using X-ray diffraction (XRD) and N_2 physisorption analyses, and Raman. The results are presented in Fig. 3.

The low-angle XRD pattern of the SBA-15 support (Fig. S2) displays well-defined diffraction peaks at 0.93°, 1.57° and 1.81°, corresponding to the (100), (110), and (200) planes characteristic of a *P6mm* hexagonal symmetry structure reflecting the well-defined hexagonal arrangement of pores in SBA-15 support.[26] The diffractogram of MoO_3@NiO/SBA-15 exhibited relatively broad peak characteristics of amorphous silica and poorly defined diffraction peaks at $\sim 2\theta$: 37.17°, 43.31°, 62.79°, 75.50° and 79.39° associated with (101), (200), (220), (311), and (222) planes of cubic NiO (JCPDS no. 01-1239).[27] No peaks of MoO_3 were observed, indicating that MoO_3 particles were amorphous or very small/highly dispersed within the SBA-15 support, as we observed in HAADF-STEM images where sub-nanometric clusters where observed (Fig. 3a). Upon the sulfidation step, no diffraction patterns related to the Ni phase were observed in the 2D/3D MoS_2@Ni/SBA-15 heterostructure and only two broad peaks observed at 33.37° and 58.79° are identified as the (100) and (110) reflections of MoS_2 in the 2H polymorph (JCPDS 37-1492) (Fig. 3a). The absence of the (002) peak at 14.4° in the 2D/3D MoS_2@Ni/SBA-15, which typically represents the periodicity of 2H-MoS_2 along the c-axis, suggests a consistent presence of few layers or predominantly mono layer MoS_2.[28]

Raman spectra (Fig. 3f) were collected to further confirm the structural transformation from the oxidic MoO_3@NiO/SBA-15 into 2D/3D MoS_2@Ni/SBA-15. The SBA-15 support exhibits no discernible Raman features within the studied range, as expected for amorphous silica.[29] For MoO_3@NiO/SBA-15, the spectrum displays several well-defined lines at 275, 330, 367, 654, 814, and 988 cm^{-1}, characteristic of molybdenum oxide species (MoO_3) dispersed over the SBA-15 surface.[30,31] Specifically, the line at 275 cm^{-1} corresponds to the bending mode of Mo═O bonds, while those at 330 and 367 cm^{-1} are attributed to Mo_3–O and Mo═O bending vibrations, respectively.[30,31] The line at 654 cm^{-1} is assigned to the Mo_3–O stretching mode, arising from triply coordinated oxygen shared among three

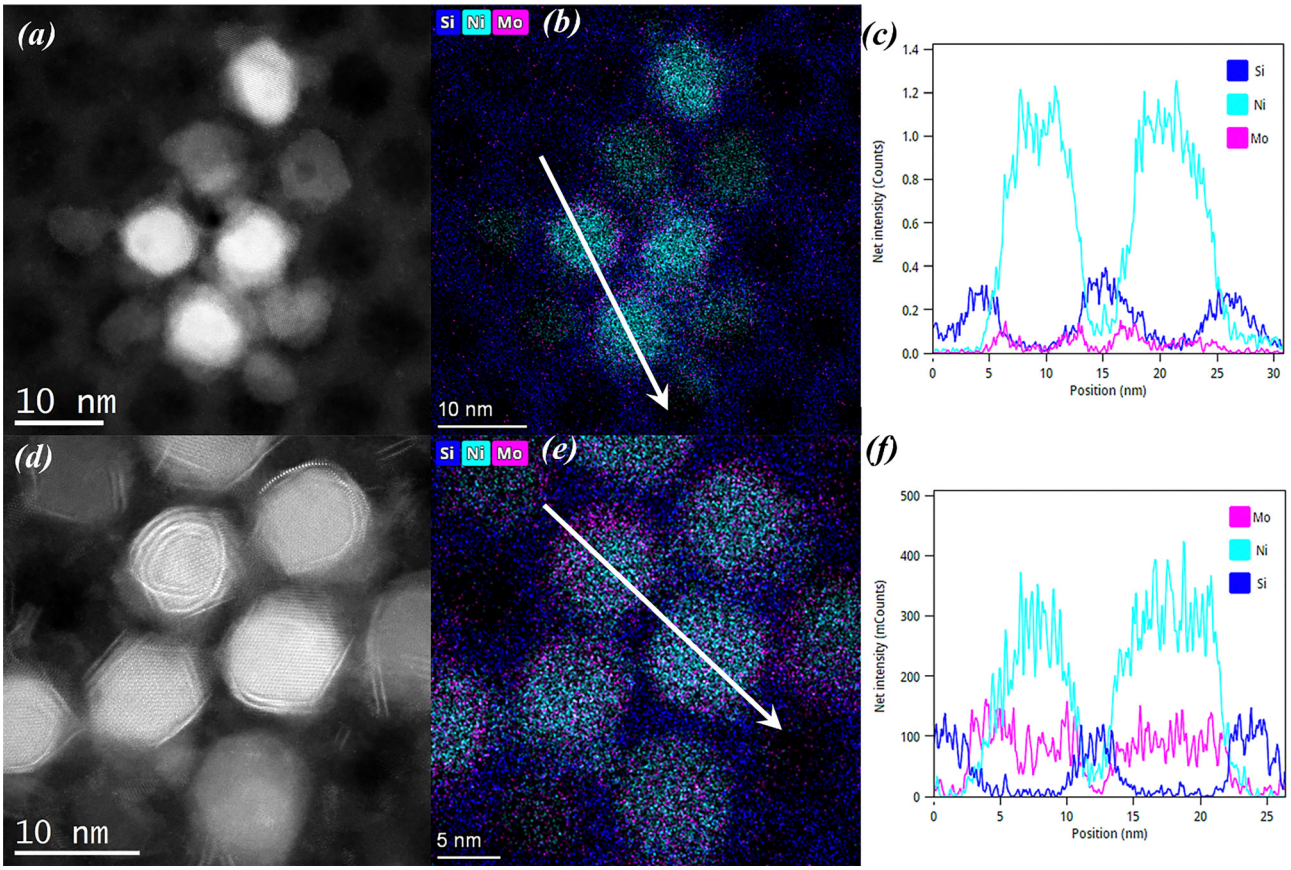

Fig. 2 STEM-HAADF image, EDS maps and EDX net intensity profile of (a)–(c) MoO_3@NiO/SBA-15 and (d)–(f) 2D/3D MoS_2@Ni/SBA-15.

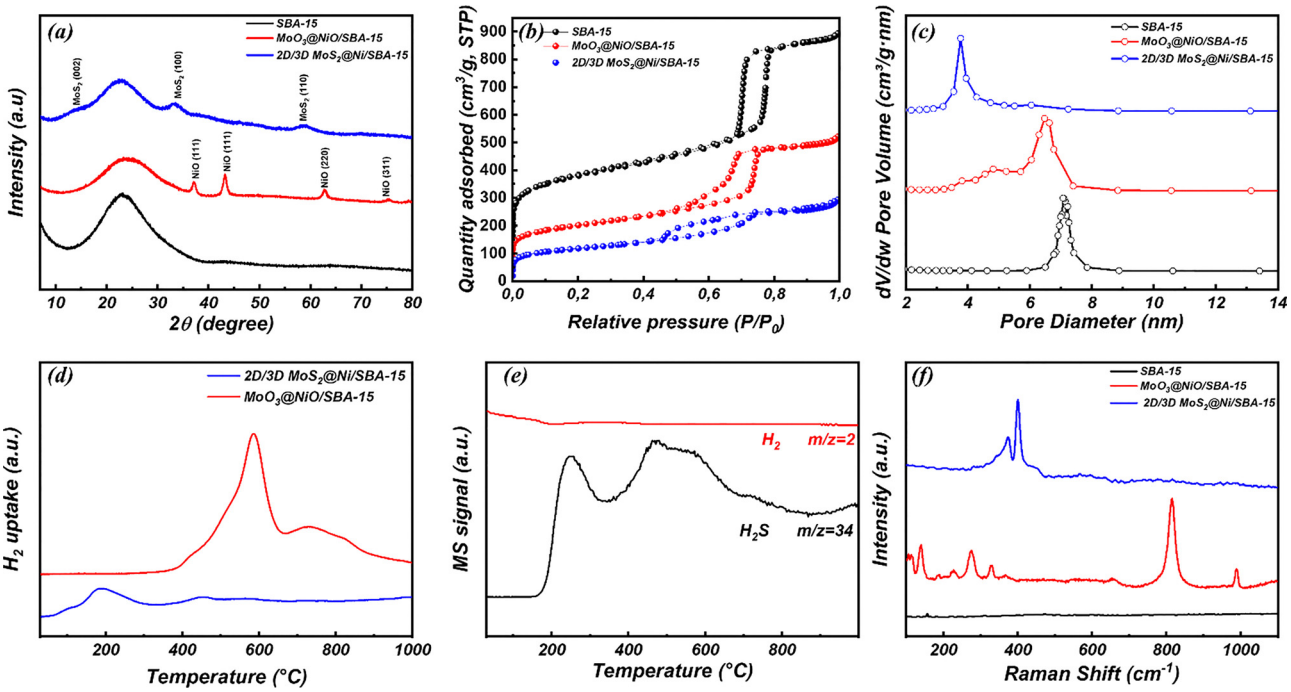

Fig. 3 (a) XRD patterns (b) nitrogen sorption isotherms and (c) corresponding pore-size distribution of SBA-15, MoO_3@NiO/SBA-15 and 2D/3D MoS_2@Ni/SBA-15, (d) H_2-TPR analysis (e) and the corresponding MS profile of 2D/3D MoS_2@Ni/SBA-15, (f) Raman spectra of SBA-15, MoO_3@NiO/SBA-15 and 2D/3D MoS_2@Ni/SBA-15.

adjacent octahedra. The 814 cm^{-1} peak originates from Mo_2–O stretching in corner-sharing octahedra, and the prominent band at 988 cm^{-1} reflects terminal Mo^{6+}═O stretching vibrations involving unshared oxygen atoms. Additional weak lines observed at 138 cm^{-1} (lattice vibrations) and at 227 cm^{-1} (Mo_2–O bending modes) further confirm the presence of MoO_3 phases.[30,31] Upon sulfidation step, the Raman spectrum of 2D/3D MoS_2@Ni/SBA-15 (Fig. 3f) reveals two distinct MoS_2 Raman shifts at 375 and 402 cm^{-1}, corresponding to the in-plane Mo–S phonon mode (E^1_{2g}), and out-of-plane Mo–S mode (A^{1g}) respectively.[32,33] This observation aligns well with the HAADF-STEM and XRD results, corroborating the formation of mono/few-layer MoS_2 on Ni-rich particles.

N_2 physisorption analysis (Fig. 3b) confirms that SBA-15, MoO_3@NiO/SBA-15, and 2D/3D MoS_2@Ni/SBA-15 heterostructure all exhibit type IV adsorption isotherms, characteristic of mesoporous materials. The SBA-15 support displays an H1-type hysteresis loop, whereas the oxidic and sulfided catalysts (MoO_3@NiO/SBA-15 and 2D/3D MoS_2@Ni/SBA-15) show H2b-type hysteresis, indicative of more complex pore structures possibly associated with partial support pore-clogging with Mo and Ni nanoparticles. The 2D/3D MoS_2@Ni/SBA-15 sample exhibits a BET surface area of 406 $m^2\ g^{-1}$, a total pore volume of 0.43 $cm^3\ g^{-1}$, and a narrow pore size distribution centred around 3–5 nm (Fig. 3c), confirming the preservation of mesoporosity after sulfidation. Compared to the pristine SBA-15 (912 $m^2\ g^{-1}$, 1.17 $cm^3\ g^{-1}$), the significant reductions in surface area and pore volume for 2D/3D MoS_2@Ni/SBA-15 catalyst confirm partial pore filling or blockage by Ni and MoS_2 species within the mesoporous structure.

Surface reactivity towards H_2

To evaluate the surface reactivity towards H_2, H_2-TPR was conducted on both the oxidic MoO_3@NiO/SBA-15 precursor and the sulfided 2D/3D MoS_2@Ni/SBA-15 heterostructure (Fig. 3d and e). The TPR profile of MoO_3@NiO/SBA-15 reveals two main reduction phenomena. A first reduction starting after 400 °C and centred around 586 °C is attributed to the reduction of Ni^{2+} to Ni^0,[34,35] and the stepwise reduction of molybdenum species from Mo^{6+} (associated with octahedrally coordinated Mo in MoO_3) to Mo^{4+}. At high temperature, a broader reduction is observed, at temperature ranging between 675 and 900 °C, which can be associated to the reduction of Mo^{4+} species to metallic Mo.[34,36]

The 2D/3D MoS_2@Ni/SBA-15 catalyst exhibits a distinct TPR profile which is associated with sulfur-based reactivity. A low-temperature, reduction observed between 70 and 300 °C corresponds to the removal of weakly bonded sulfur species, likely originating from disulfide (S_2^{2-}) units located at the edges of MoS_2 slabs. As the temperature increases, a broader reduction feature appears in the range of 400–600 °C, which is associated with the gradual removal of strongly bonded sulfur atoms within the MoS_2 lattice, including those from both edge and basal plane sites.[37] Notably, both reduction steps are accompanied with the production of H_2S, as evidenced by the corresponding MS signals (Fig. 3d and e). This H_2S production supports the occurrence of hydrogen sulfur surface reactions: Li *et al.*[38] proposed that the formation of sulfur vacancies on MoS_2 surfaces may result from the interaction of adsorbed hydrogen with sulfur atoms, leading to H_2S formation.

Surface chemical states over 2D/3D MoS_2@Ni/SBA-15

X-ray photoelectron spectroscopy (XPS) was performed to study the extent of sulfidation process and characterise the evolution of the chemical states and surface composition of the oxidic precursor and 2D/3D MoS_2@Ni/SBA-15 heterostructure. The results are presented in Fig. 4.

As expected, the full XPS survey shown in Fig. 4a and d displays the characteristic signals of Ni, O, Mo, and Si elements for both samples, while an additional peak corresponding to sulfur is clearly observed in the 2D/3D MoS_2@Ni/SBA-15 catalyst. The high-resolution Mo 3d spectrum of the MoO_3@NiO/SBA-15 catalyst (Fig. 4b) shows two distinct peaks at 233.3 eV and 236.5 eV, which correspond to the Mo $3d_{5/2}$ and Mo $3d_{3/2}$ binding energies, respectively. These values are in good agreement with those reported in the literature for Mo^{6+} species in MoO_3 phase.[39]

In the Ni 2p region (Fig. 4c), the two main signals at 855.8 eV and 873.3 eV (Ni $2p_{3/2}$ and Ni $2p_{1/2}$) along with shake-up satellites at 861.0 eV and 879.8 eV, are indicative of the presence of Ni^{2+}.[40] Then, no signal corresponding to metallic Ni or Mo was detected, confirming the oxidic nature of the material.

Upon sulfidation at 400 °C, the surface chemistry changes markedly, as shown in the spectra of 2D/3D MoS_2@Ni/SBA-15 (Fig. 4d–f). The Mo 3d region exhibits a clear shift to lower binding energies, with three distinct doublets corresponding to different oxidation states of molybdenum. The first doublet, located at 229.4 eV (Mo $3d_{5/2}$) and 232.6 eV (Mo $3d_{3/2}$), is attributed to Mo^{4+} in the 2H-MoS_2 phase. A second doublet, observed at 230.6 eV and 233.7 eV, corresponds to Mo^{5+}, while the third at 233.8 eV and 236.7 eV, is assigned to Mo^{6+}. These features indicate the presence of partially oxidized Mo species.[41,42] Moreover, the presence of the S 2s peak characteristic of Mo–S bond, is also observed in this spectral range. Two sulfur species were identified, with binding energies at 226.4 eV corresponding to S^{2-} in MoS_2, and at 227.4 eV, attributed to S^- species (S 2p region is presented in Fig. S3).[43] The high-resolution Ni 2p spectra of 2D/3D MoS_2@Ni/SBA-15 confirmed the presence of both metallic Ni^0 and Ni^{2+}. The signal at binding energies of 853.1 and 854.5 eV are identified as metallic Ni^0 and Ni^{2+}, while peaks at 860.1 and 880.0 eV are attributed to Ni^{2+} shake-up satellites.[44] No additional features indicative of Ni–S bonding were observed; however, the presence of very small amounts of Ni–S interfacial species at the MoS_2–Ni contact points cannot be fully excluded and may contribute synergistically to the catalytic behaviour.[45]

Catalytic performance and stability in CO_2 hydrogenation reaction

The catalytic performance of MoO_3@NiO/SBA-15 and 2D/3D MoS_2@Ni/SBA-15 was evaluated under hydrogen-rich conditions,

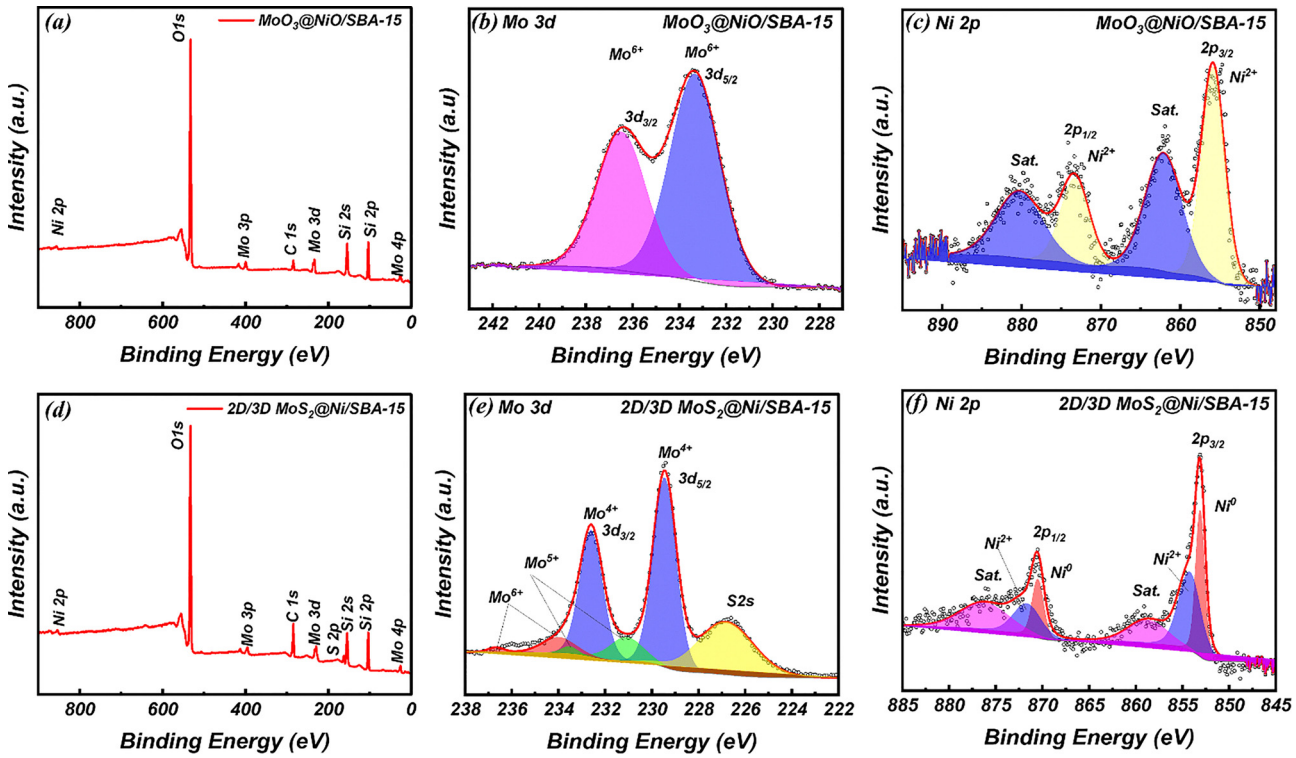

Fig. 4 (a) X-ray photoelectron survey spectrum, (b) Mo 3d region and (c) Ni 2p region of MoO3@NiO/SBA-15; (d) X-ray photoelectron survey spectrum and (e) Mo 3d region and (f) Ni 2p region of 2D/3D MoS2@Ni/SBA-15.

i.e., CO_2/H_2 ratio of 1/4 at temperature range 200–800 °C and at WHSV = 12 000 mL g^{-1} h^{-1}. The results of catalytic activity, selectivity towards CO or CH_4, and stability are presented in Fig. 5.

At the test conditions, both MoO_3@NiO/SBA-15 and 2D/3D MoS_2@Ni/SBA-15 showed high CO_2 conversion which increased readily with increasing temperature (Fig. 5a). At low temperatures, MoO_3@NiO/SBA-15 exhibited a higher conversion rate than MoS_2@Ni/SBA-15. For instance, at 400 °C, the CO_2 conversion over MoO_3@NiO/SBA-15 was 30%, while it was of only 7% CO_2 conversion over 2D/3D MoS_2@Ni/SBA-15. However, at 600 °C and above, both catalysts operated at near thermodynamic conversion.

The differences between MoO_3@NiO/SBA-15 and 2D/3D MoS_2@Ni/SBA-15 are much more pronounced when the selectivity towards methanation of CO_2 or reduction to CO is considered. At low temperatures, below 400 °C, a methane selectivity of ~99% was achieved on MoO_3@NiO/SBA-15. Increasing further the reaction temperature results in switching the selectivity towards CO production, which is the thermodynamically favoured product at higher temperatures: a selectivity of ~100% to CO is achieved at 700 °C (Fig. 5b). Surprisingly, the 2D/3D MoS_2@Ni/SBA-15 catalyst shows complete suppression of CH_4 formation across the entire reaction temperature range, Fig. 5c, with complete selectivity towards CO formation even at low temperature. This distinct selectivity behaviour highlights the inhibition of Ni-driven methanation in the MoS_2-encapsulated system, likely due to electronic and geometric confinement effects imposed by the MoS_2 layers.

In terms of activity and selectivity, 2D/3D MoS_2@Ni/SBA-15 reported here shows enhanced performances with respect to Mo-based catalysts from the literature. For instance, at 500 °C, H_2/CO_2 = 4 : 1, and WHSV = 12 000 mL g^{-1} h^{-1} the catalyst achieved a CO_2 conversion of 33.3% with 100% selectivity towards CO. To contextualize these results, Zhang *et al.*[46] investigated a series of supported MoP catalysts (Mo–P–SiO_2, Mo–P–Al_2O_3, and Mo–P–CeAl) under identical reaction conditions (500 °C, H_2/CO_2 = 4 : 1, WHSV = 12 000 mL g^{-1} h^{-1}). These catalysts exhibited lower conversion rates (13%, 15.5% and 14.4%, respectively), along with reduced CO selectivity (97.5%, 85.8% and 89.2%). This clearly highlights the superior performance of the MoS_2@Ni/SBA-15 heterostructure for both CO selectivity and conversion rate. Similarly, Zhuang *et al.*[47] reported that the commercial Cu/ZnO/Al_2O_3 catalyst achieved only 17% CO_2 conversion at 500 °C under a much higher WHSV of 90 000 mL g^{-1} h^{-1}. Authors demonstrated that Ru promotion (0.5 wt%) was required to enhance the catalytic activity, which allowed them to reach a conversion of 46% at the same temperature. Additionally, Querido *et al.*[48] compared several Cu-based catalysts under RWGS conditions (WHSV = 60 000 mL g^{-1} h^{-1}, CO_2 : H_2 = 1 : 4). The reference Cu/ZnO catalyst achieved a CO_2 conversion of 34.9% at 600 °C, outperforming catalysts supported on pristine carbon materials. Specifically, CNT-supported catalysts showed 17.6% conversion, while those on activated carbon reached only 10.4%, all with 100% CO selectivity. Beyond Mo- and Cu-based catalysts, it is also relevant to compare these results with Ni-based

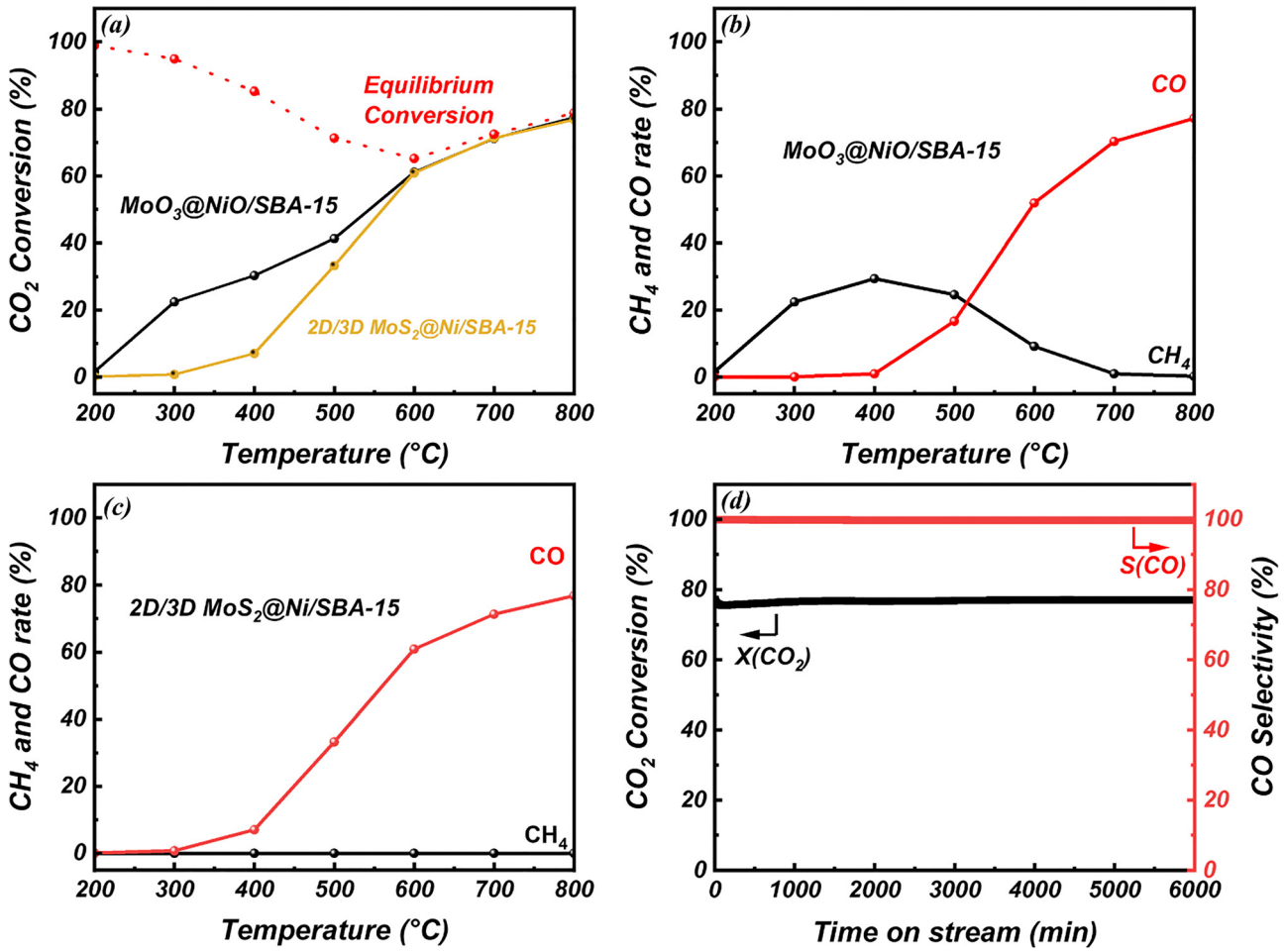

Fig. 5 (a) CO_2 conversion; formation of CO and CH_4 for (b) MoO_3@NiO/SBA-15, and (c) for 2D/3D MoS_2@Ni/SBA-15 catalysts for a temperature ramp from 200 to 800 °C with a gas mixture of 1 : 4 (CO_2 : H_2) and WHSV = 12 000 mL g^{-1} h^{-1}; (d) stability test for 2D/3D MoS_2@Ni/SBA-15.

systems known for their tunable methanation and RWGS activity. For instance, Zhang *et al.*[45] reported that Ni/ZrO_2 exhibited 100% CO selectivity at 500 °C. In their study, the catalyst was intentionally modified with trace sulfur species, generating surface sulfates and sulfur–carbonate intermediates that strongly suppress methanation capability of the Ni-catalyst. Indeed, sulfur poisons the hydrogenation Ni-sites, inhibiting formate hydrogenation and thereby steering the reaction toward CO formation, as demonstrated by Gac *et al.*[49] Here, MoO_3@NiO/SBA-15 catalyst display the classical behavior expected for metallic Ni catalyst, namely predominant methane formation at low temperature and mixed CO/CH_4 selectivity at high temperature: at 500 °C our catalyst yields 40.4% CO and 59.6% CH_4, consistent with well-established trends for unmodified Ni-based catalysts.[50] A comparative overview of CO_2 conversion and CO selectivity for the synthesized catalysts and previously reported Mo-based systems is provided in Table 1. All these comparisons demonstrate the competitive performances of the 2D/3D MoS_2@Ni/SBA-15 catalyst, particularly considering its high CO_2 conversion rate and complete CO selectivity at a relatively moderate temperature. Finally, a stability test was performed over 100 h on stream at 800 °C (Fig. 5d). The sulfided catalyst exhibited excellent durability, maintaining > 75% CO_2 conversion and 100% CO selectivity without any signs of deactivation.

Studies have shown that tuning the dispersion, particle size, and electronic environment of Ni plays a decisive role in steering selectivity between methanation and RWGS pathway. Increasing Ni dispersion, lowering Ni loading, introducing a second metal to generate bimetallic interfaces, and strengthening metal–support interactions have all been identified as effective strategies to enhance CO selectivity.[56–58]

For example, Wu *et al.*[59] reported that varying Ni loadings on SiO_2 (0.5 to 10 wt%) modulates surface hydrogen coverage, which directly shifts the balance between CO and CH_4 formation. Similar trends were observed on Ni/MgO,[60] Ni/CeO_2,[61] and Ni/Al_2O_3,[62] where low Ni loading was consistently associated with improved RWGS performance. In our system, the use of ordered mesoporous SBA-15 support provides a high surface area and uniform mesopore size that favour the formation of highly dispersed Ni nanoparticles. More importantly, the incorporation of Mo as a second metal further modifies the system properties by introducing Ni–Mo interactions. Upon sulfidation, these interactions deepen through the formation

Table 1 Comparison of CO_2 conversion and CO selectivity for the synthesized Mo-based catalysts and literature reported catalysts

	500 °C		700 °C		
Catalyst	CO_2 conversion (%)	CO selectivity (%)	CO_2 conversion (%)	CO selectivity (%)	Ref.
MoO_3@NiO/SBA-15	41,3	40.4	71.23%	98.6%	This work
2D/3D MoS_2@Ni/SBA-15	33.2	100	71.32%	100%	This work
Mo-P-SiO_2	13	97.5	61.3%	88.4%	46
Mo-P-Al_2O_3	15.5	85.8	57.8%	83.7%	46
Mo-P-CeAl	14.4	89.2	54.8%	87.1%	46
20%Cu-Ni/γ-Al_2O_3	23.2	75.5	28.7%	79.7%	51
β-Mo_2C	∼5	100	n.a	n.a	52
Cu/β-Mo_2C	∼30	99	n.a	n.a	52
Ni/ZrO_2	27.6	100	n.a	n.a	45
Mo/FAU	14.3	99	n.a	n.a	53
Ni(1)/FAU	17.2	45	n.a	n.a	53
Ni/CeO_2–Al_2O_3	∼63	∼13	∼67%	∼94%	54
Ni/Al_2O_3	28	49	n.a	n.a	55

of Ni–Mo_x interfacial sites. Such interfacial domains can alter the electronic structure of Ni, reducing its hydrogenation capacity and weakening C–O bond cleavage, which collectively suppress methane formation. Consequently, the reaction pathway shifts toward CO formation even under conditions where Ni would predominantly favour methanation.

Therefore, the reaction mechanism in our catalysts is governed by the synergistic interplay between Ni dispersion (enhanced over SBA-15) and Ni–Mo electronic interactions. This explains why a reaction pathway dominated by RWGS is obtained.

Reaction induced carbonization: how the nature of the active site evolves during the reaction

Reconstruction of catalyst surfaces under reactive environments, *e.g. in situ* transformations, can result in the formation of active or selective phases under reaction conditions, a central concept in modern heterogeneous catalysis.[63,64] This is particularly relevant for molybdenum-based system which can accommodate a variety of heteroatoms including oxygen, carbon, nitrogen, and phosphorus within its crystalline framework, thereby enabling phase evolution under reactive atmospheres.[65,66] In the context of the RWGS reaction, we will confirm that both the 2D/3D MoS_2@Ni/SBA-15 and MoO_3@NiO/SBA-15 heterostructures underwent structural transformations upon prolonged exposure to CO_2/H_2 mixtures under reaction conditions.

After 100 h on stream at 800 °C, post-reaction characterisation of MoS_2@Ni/SBA-15 reveals a phase transformation from the initial MoS_2 and MoO_3 phases into crystalline β-Mo_2C phase, as evidenced by XRD (Fig. 6a), alongside the reduction of NiO to metallic Ni: the diffraction peaks at 2θ = 34.5°, 38.0°, 39.5°, 52.3°, 61.8°, 69.7°, and 74.9, are well aligned with the (100), (002), (101), (102), (110), (103), and (112) planes of β-Mo_2C phase (JCPDS PDF No. 65-8766);[67,68] diffraction peaks at 2θ = 43.7° and 50.9°, correspond to the (111) and (200) planes of metallic Ni (JCPDS PDF No. 04-0850).[69]

Importantly, the emergence of the carbide reflections even after reaction at lower temperatures (Fig. S4) indicates that the MoS_2-derived catalyst begins carburizing as early as ∼200 °C, whereas the MoO_3-derived catalyst requires temperatures closer to ∼400 °C to initiate a similar transformation. This difference is consistent with the higher mobility of sulfur, which facilitate earlier hydrodesulfurization and carbon incorporation. Such behavior agrees well with recent studies by Du *et al.*,[70] who demonstrated the stepwise removal of oxygen from oxide and subsequent carbon uptake leading to MoC_x formation under RWGS conditions, and by Jeon *et al.*, who showed that MoS_2 can be converted into Mo_2C through sequential desulfurization and carbide nucleation starting from its edge sites.[71]

The 2D/3D MoS_2@Ni/SBA-15 structural evolution has been also confirmed by CHNS elemental analysis (Fig. 6c), which shows a significant decrease in sulfur content accompanied by an increase in carbon content, confirming the carburisation of Mo under the reaction environment. The carburization process was accompanied by a slight decrease in surface area and pore volume (342 $m^2\ g^{-1}$ and 417 $m^2\ g^{-1}$ for post reaction 2D/3D MoS_2@Ni/SBA-15 and MoO_3@NiO/SBA-15 catalysts respectively) as it can be seen from the results of N_2 physisorption isotherm (Fig. 6b).

The evolution of the surface properties, namely oxidation state and chemical composition, was further investigated by XPS (Fig. 6d–f). Upon reaction, the high-resolution Mo 3d XPS spectra of both the 2D/3D MoS_2@Ni/SBA-15 and MoO_3@NiO/SBA-15 catalysts reveal significant change in surface chemistry, consistent with *in situ* carburization mechanism under RWGS conditions. Notably, a new doublet is observed at binding energies of 228.4 eV and 231.5 eV for 2D/3D MoS_2@Ni/SBA-15, and at 228.4 eV and 231.6 eV for the MoO_3@NiO/SBA-15. It corresponds to Mo $3d_{5/2}$ and Mo $3d_{3/2}$ signal of Mo^{2+} species. These signals are characteristic of β-Mo_2C, confirming the formation of molybdenum carbide.[72,73] In addition, doublets at 229.2 eV and 232.4 eV for 2D/3D MoS_2@Ni/SBA-15 and at 229.5 eV and 232.5 eV for the MoO_3@NiO/SBA-15, shows partially reduced Mo species ($Mo^{\delta+}$, with $2 < \delta < 4$). Additionally, both catalysts exhibit a high binding energy doublet at 232.6 eV and 235.8 eV, characteristic of Mo^{6+}.

For the 2D/3D MoS_2@Ni/SBA-15 catalyst, Mo_2C appears to be the predominant surface species (47 at%), accompanied by minor contributions from Mo^{6+} (26.7 at%) and partially oxidized $Mo^{\delta+}$ species (26.15 at%): it indicates an incomplete

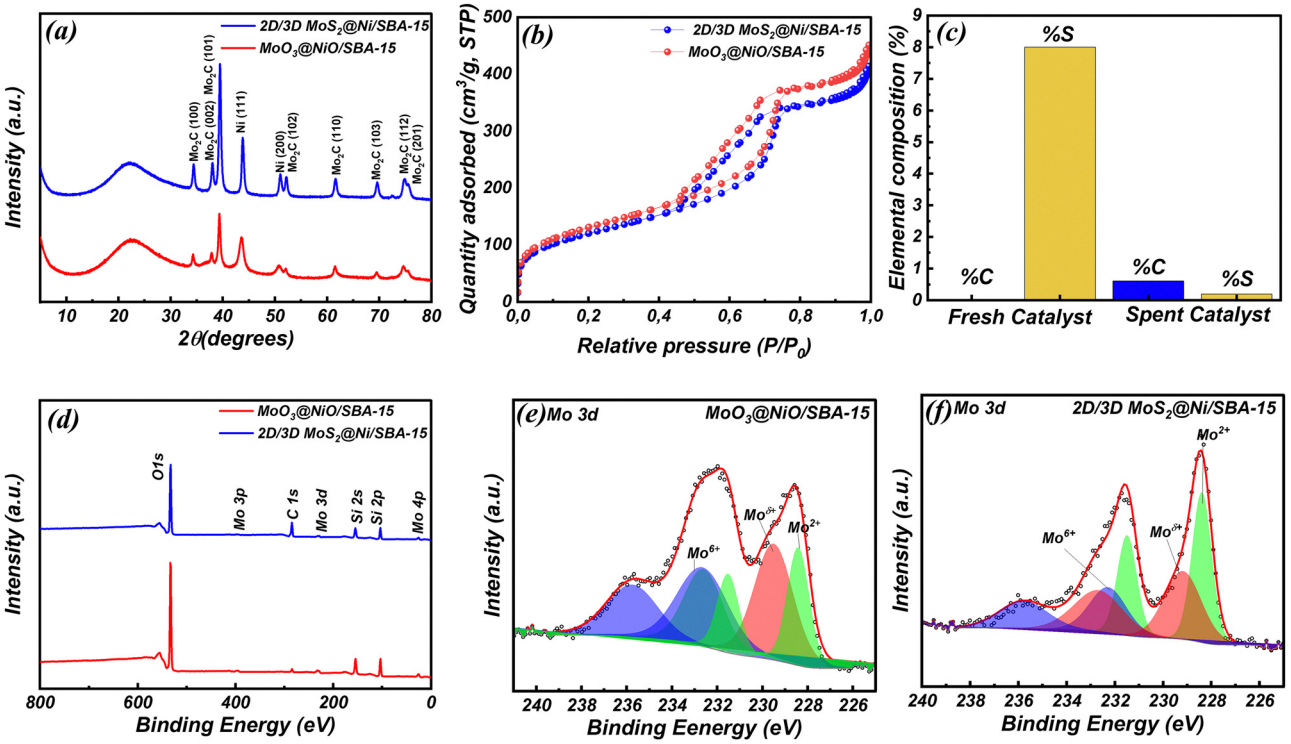

Fig. 6 (a) XRD patterns, (b) nitrogen adsorption/desorption isotherms, (c) CHNS analysis of the fresh and spent 2D/3D MoS_2@Ni/SBA-15 catalyst, (d) X-ray photoelectron survey spectrum, and (e) and (f) High-resolution spectra of the Mo 3d core level for the spent MoO_3@NiO/SBA-15 and 2D/3D MoS_2@Ni/SBA-15 catalysts.

carburization and possible surface reoxidation. In contrast, the MoO_3@NiO/SBA-15 sample was primarily oxidized, with Mo^{6+} and Mo^{δ}+ species accounting for 36.3 at% and 37.0 at% of the total Mo content, respectively. The major contribution of the oxidized species in this case may be attributed to surface passivation (likely due to air exposure during sample handling and transfer for analysis, which can lead to partial reoxidation of carbide phases).

The Ni 2p XPS spectra of the post-reaction MoO_3@NiO/SBA-15 and MoS_2@Ni/SBA-15 catalysts are shown in Fig. S5. For both materials, the Ni $2p_{3/2}$ region can be decomposed into three main components located at binding energies of 852.7, 855.4, and 856.9 eV for MoO_3@NiO/SBA-15, and at 852.8, 855.5, and 856.8 eV for 2D/3D MoS_2@Ni/SBA-15. Signals are assigned to metallic Ni^0, Ni–C_x species, and oxidized Ni species, respectively.[74,75] The presence of the Ni–C_x contribution indicates partial carburization of Ni under RWGS conditions, consistent with the formation of Ni–Mo mixed carbides. In addition, characteristic shake-up satellite features associated with Ni^{2+} species are observed at higher binding energies, confirming the coexistence of residual oxidized Ni at the catalyst surface.

To elucidate the electronic interplay between Ni and Mo species within the 2D/3D MoS_2@Ni/SBA-15 architecture, X-ray photoelectron spectroscopy was employed to compare the Mo 3d core-level spectra of the Ni-containing catalyst and its Ni-free counterpart (MoS_2/SBA-15) after *in situ* carburization. As shown in Fig. S6, both samples exhibit characteristic MoC_x features in the Mo 3d region. However, the Mo $3d_{5/2}$ peak of MoC_x in the Ni-containing 2D/3D MoS_2@Ni/SBA-15 appears at a lower binding energy (228.4 eV) compared to that of the Ni-free MoS_2/SBA-15 (228.6 eV). This shift of 0.2 eV toward lower binding energy indicates a charge transfer from Ni to the MoC_x phase, confirming the modification of the electronic environment of Mo induced by Ni incorporation.[23] Such interfacial electron transfer is expected to have important implications for the electronic structure and catalytic behaviour of the MoC_x phase.

To investigate the morphological evolution of the catalyst under reaction conditions, STEM-HAADF imaging was performed on the 2D/3D MoS_2@Ni/SBA-15 catalyst after 100 hours of RWGS reaction (Fig. 7a–d and Fig. S7, S8). As depicted in Fig. 7b, Ni nanoparticles remained homogeneously dispersed across the SBA-15 support, with an average particle size of approximately 10.0 ± 0.5 nm. This minimal growth in particle size confirms the excellent thermal stability and resistance to sintering of Ni under prolonged high-temperature RWGS conditions (800 °C), likely due to physical spatial confinement of Ni within the layered MoS_2 matrix and between silica walls. A particularly noteworthy observation is presented in Fig. 7c and d, where a Mo-rich layered structure with an interplanar spacing of approximately 4.8 Å is clearly resolved. This atomic spacing corresponds to the (002) plane of β-Mo_2C,[71] aligning with reported crystallographic data for the c-axis lattice parameter of 2D-Mo_2C.[71]

The emergence of these well-ordered, lamellar Mo_2C domains strongly suggests a topotactic transformation of MoS_2 into Mo_2C

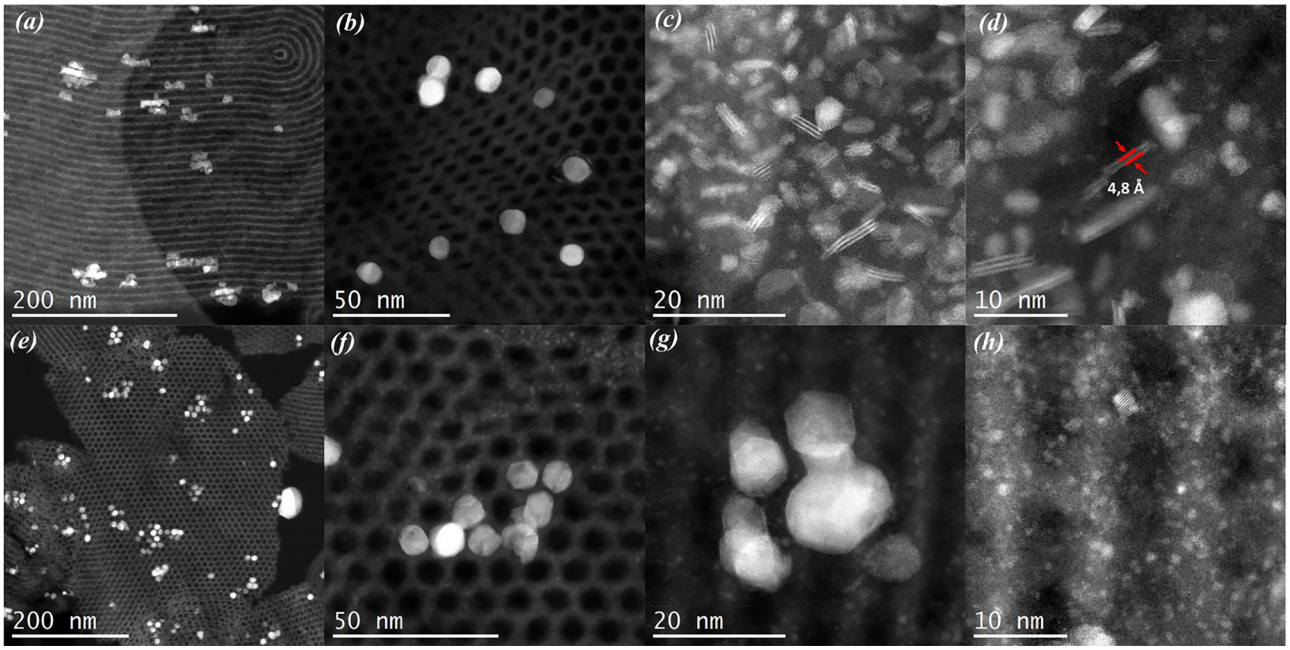

Fig. 7 (a)–(d) HAADF images for the spent 2D/3D MoS_2@Ni/SBA-15, and (e)–(h) spent MoO_3@NiO/SBA-15.

during the carburization process under reaction conditions. This transformation appears to preserve the original 2D morphology of MoS_2, facilitating the formation of sheet-like 2D-Mo_2C, which is known for its enhanced catalytic and electronic properties.[76]

The STEM images of the post-reaction MoO_3@NiO/SBA-15 catalyst (Fig. 7e–h) reveal substantial changes in metal dispersion. Notably, sintering of Ni nanoparticles appears evident in a few areas (Fig. 7g), with the formation of larger particles/agglomerates after exposure to high-temperature RWGS conditions for 100 hours, even though this is not visible by XRD. It therefore demonstrates that this phenomenon remains limited. The images highlight the formation and spatial distribution of the Mo-containing phase, which appears clearly localized along the silica walls. This observation indicates the formation of Mo-carbide species preferentially at the outer mesoporous framework rather than within the pores.

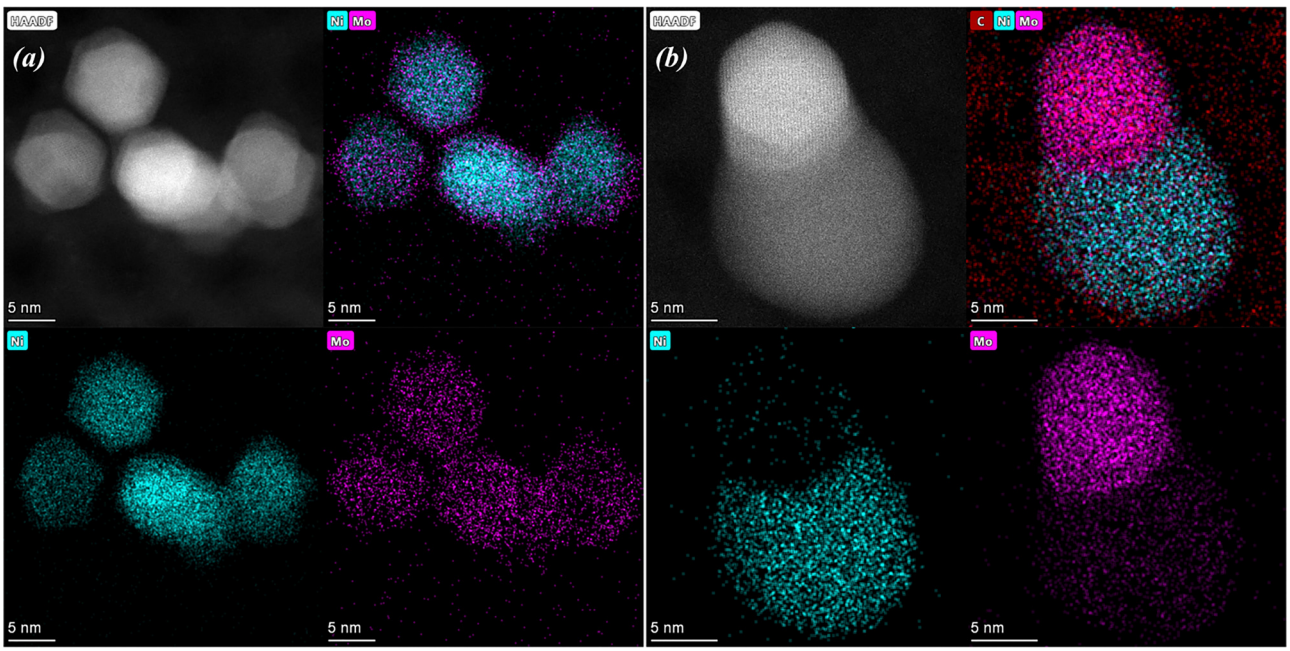

Fig. 8 STEM-HAADF and EDS elemental mapping analysis of spent (a) MoO_3@NiO/SBA-15 and (b) 2D/3D MoS_2@Ni/SBA-15 catalysts after 100 h of time-on-stream in RWGS conditions.

To further support the morphological observations derived from STEM-HAADF analysis, EDS element mapping was conducted on post-reaction MoO_3@NiO/SBA-15 and 2D/3D MoS_2@Ni/SBA-15 (Fig. 8a and b). For the MoO_3@NiO/SBA-15 catalyst (Fig. 8a), the EDS maps reveal a significant spatial overlap between Ni and Mo signals on large 5–10 nm objects, suggesting intermixing of Ni and Mo species. The HAADF image reveals relatively large and aggregated nanoparticles, consistent with the sintering of Ni particles observed after 100 hours on stream at high temperature. In contrast, in the case of the post-reaction 2D/3D MoS_2@Ni/SBA-15 catalyst, the STEM-HAADF and EDS mapping reveal a distinctive spatial arrangement of Ni and Mo species. Unlike classical core–shell or fully encapsulated morphologies, where Ni nanoparticles are entirely confined within a Mo-based matrix, the Ni and Mo signals are only partially overlapping. Ni-rich domains are clearly visible and remain distinct from Mo-rich regions, although the two phases are not completely segregated.

This suggests a semi-integrated architecture wherein the Ni nanoparticles are in close interfacial contact with Mo-based species. While the evolution of the catalyst textural, structural, and morphological properties has been thoroughly confirmed, its potential impact on reactivity and selectivity, particularly in the low-temperature regime, remains a legitimate concern. Structural transformations during prolonged high-temperature exposure can alter active site distribution or surface accessibility, potentially compromising catalytic performance in terms of activity but also selectivity. As shown in Fig. 9, upon studying the performance in a second reaction cycle for 2D/3D MoS_2@Ni/SBA-15, the catalyst was observed to maintains 100% CO selectivity across the full temperature range, indicating that methanation pathways remain effectively suppressed upon the carburisation of Mo–S species to Mo–C species. However, a moderate decline in CO_2 conversion is observed, especially at temperatures ranges between 400–700 °C, suggesting a possible reduction in active site density. This loss of activity, despite preserving selectivity, highlights the complex interplay between structural stability and catalytic functionality. Nonetheless, the system demonstrates strong resistance to methanation and excellent selectivity retention, confirming its viability for long-term CO_2-to-CO conversion.

To investigate the structure–activity relationship of the MoO_3@NiO/SBA-15 oxide catalyst, three temperature programs (runs 1 to 4) were conducted under RWGS conditions, examining the evolution of the catalytic activity and selectivity at both high and low temperatures. The results are presented in Fig. 10. When MoO_3@NiO/SBA-15 is studied at conditions that did not favour the carburisation process (run 1–2, at temperatures not exceeding 400 °C), the catalyst remains selective towards CH_4, indicating strong hydrogenation activity as could be awaited for metallic Ni sites. However, once the reaction is conducted at higher temperatures (up to 800 °C) where the carburisation is activated (run 3–4), a clear shift in selectivity towards CO is observed. The extent of selectivity to CO can be correlated with the carburisation degree of Mo. Nevertheless, even after 2 cycles at high temperatures, the MoO_3@NiO/SBA-15 was not fully selective towards CO at low temperature (87% CO selectivity at 500 °C, Run 4). This switch in selectivity from CH_4 to CO highlights a strong structure–activity relationship: the oxide phase promotes methanation due to its high hydrogenation ability of individual Ni, while the carbide phase selectively catalyses the RWGS reaction with minimal CH_4 formation.

Importantly, the selectivity shift observed after carburization can be directly attributed to the formation of Ni–Mo mixed carbides sites. Post-reaction characterization of MoO_3@NiO/SBA-15 shows that Ni no longer persists as isolated metallic nanoparticles. Instead, a close interfacial contact develops between Ni and β-Mo_2C domains, as observed in comparative HAADF-STEM images (Fig. S9): in the fresh catalyst, Ni is homogeneously dispersed within the SBA-15 mesopores while Mo species are mainly located within the silica walls, resulting in limited contact between MoO_3 and NiO. After reaction, the particles become larger and more defined, and Ni and Mo are co-located within the same nanodomains. It indicates pronounced structural reconstruction and formation of Ni–Mo mixed carbides under RWGS conditions.

Such Ni–Mo carbides interfaces are recognized to induce strong catalytic modifications. Electron transfer between Ni and Mo_2C modifies the electronic structure of Ni, weakens hydrogenation pathways leading to CH_4 formation, and alters the adsorption energies of key reaction intermediates.[74,77] This interpretation is corroborated by the work of Galhardo *et al.*,[78] who demonstrated that conventional supported Ni catalysts undergo a drastic selectivity switch from CH_4 to CO after high-temperature CO_2 hydrogenation due to the formation of a

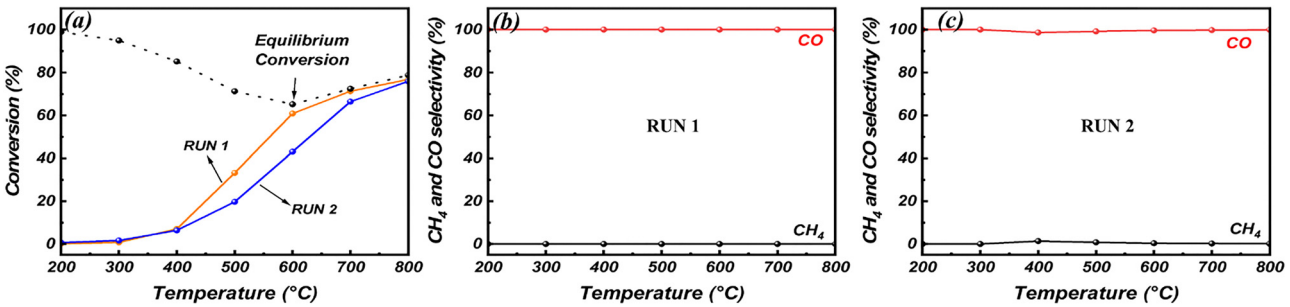

Fig. 9 (a) CO_2 conversion in run 1 and run 2 2D/3D MoS_2@Ni/SBA-15 and (b) and (c) CO and CH_4 selectivity in run 1 and run 2 respectively for a temperature ramp from 200 to 800 °C with a gas mixture of 1 : 4 (CO_2 : H_2) and WHSV = 12 000 mL g^{-1} h^{-1}.

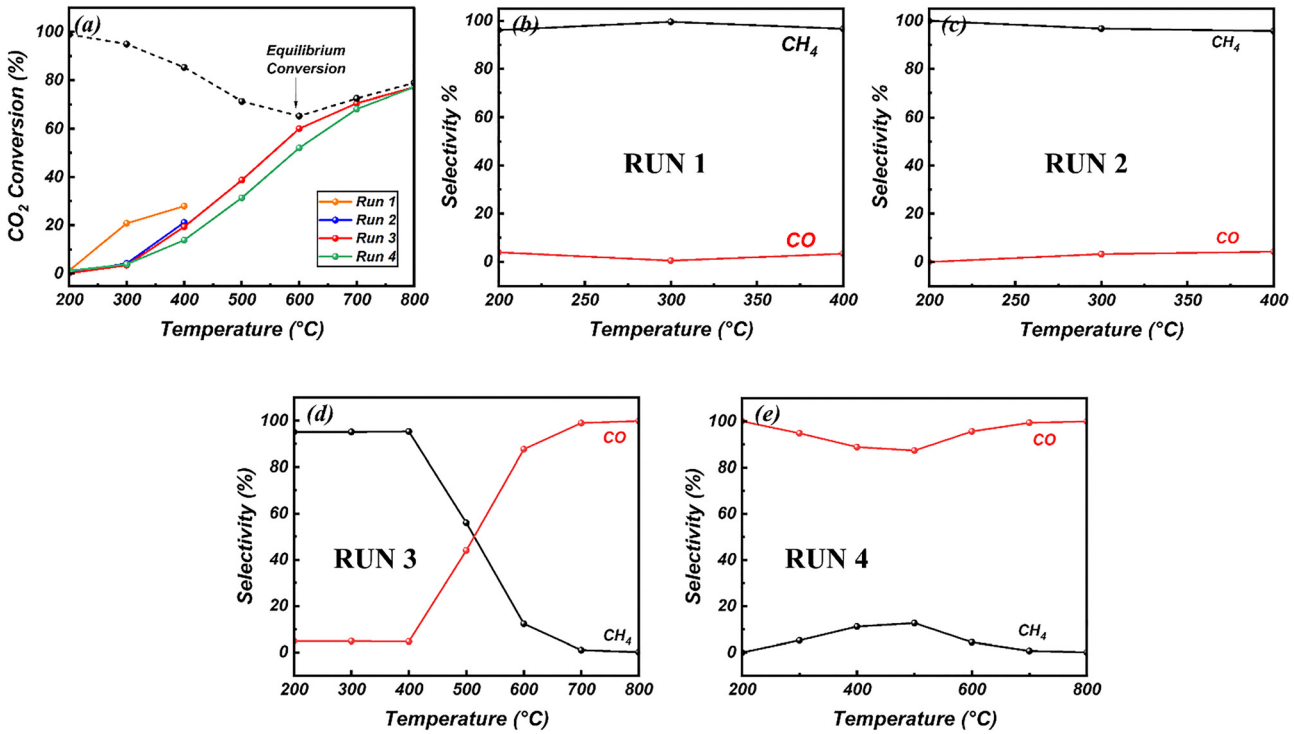

Fig. 10 (a) CO_2 conversion in MoO_3@NiO/SBA-15 at different cycles and (b)–(d) CO and CH_4 selectivity. Reaction conditions: gas mixture of 1 : 4 (CO_2 : H_2) and WHSV = 12 000 mL g^{-1} h^{-1}.

nickel carbide-like surface. *In situ* spectroscopic analysis revealed that carbon accumulation at elevated temperatures generates a carbide-like Ni phase able to stabilize a higher fraction of weakly adsorbed CO species compared to metallic Ni, thereby favouring CO desorption and suppressing methanation pathway.

In the present catalytic system, this effect is further amplified by the presence of Mo_2C, which stabilizes the carburized environment and promotes the formation of well-defined Ni-Mo mixed carbides. These interfaces stabilize undercoordinated $Ni^{\delta+}$ species as evidenced by XPS, where Ni primarily facilitates H_2 activation while Mo_2C favours CO desorption. Consequently, the cooperative interaction between Ni and Mo_2C provides an adapted environment for the suppression of CH_4 formation and the enhanced RWGS selectivity.

The unique catalytic performance of molybdenum carbide catalysts is mainly due to the incorporation of carbon into the molybdenum crystal structure. It modifies the electronic characteristics of the d-band of molybdenum carbide, making its properties similar to those of noble metals such as ruthenium.[79,80] In addition, recent studies have shown that molybdenum carbide, as a bifunctional material, can activate CO_2 by breaking the C═O bond and dissociate H_2 molecules. This dual functionality makes molybdenum carbide one attractive phase for the RWGS reaction.[81,82] However, controlling the crystallographic phase of the final product while minimizing excessive carbon deposition necessitates multistep preparation processes or the use of precious precursors and co-reagents.[83,84] This results in complex synthetic pathways that are difficult to control and extrapolate.[85] In this work, the dynamic structural evolution of NiMo sulfide and NiMo oxide-based catalysts into a NiMo carbide-based catalyst provides a pathway for the development of facile synthesis routes for nano-Mo_2C with structural properties affording full CO-selective CO_2 reduction.

Conclusions

This study demonstrates that the structural evolution of Ni–Mo-based catalysts can be purposely controlled to tune activity and selectivity during CO_2 hydrogenation. The MoO_3@NiO/SBA-15 oxide precursor exhibits high CO_2 conversion but methanation is favoured at low temperature due to the strong hydrogenation activity of metallic Ni sites. Upon gas-phase sulfidation, the heterostructure undergoes a profound transformation, yielding 2D/3D MoS_2@Ni/SBA-15 with ultrathin MoS_2 nanosheets intimately associated with Ni nanoparticles. XPS analysis further confirmed electron transfer from Ni to Mo by comparing the 2D/3D MoS_2@Ni/SBA-15 with a Ni-free MoS_2 catalyst, where a shift of the Mo 3d binding energy to lower values was observed, indicating modification of the Mo electronic state. This configuration effectively suppresses Ni-driven methanation and ensures 100% selectivity towards CO across the full temperature range studied. At 500 °C, the catalyst achieves a CO_2 conversion of 33.3% with complete CO selectivity, outperforming most state-of-the-art transition metal catalysts reported in the literature.

Under prolonged RWGS conditions at 800 °C, the MoS_2@Ni/SBA-15 undergoes further *in situ* carburisation, forming Ni–Mo mixed carbides while maintaining structural stability and limiting Ni sintering. This dynamic evolution enhances stability, with the catalyst sustaining >75% CO_2 conversion and complete CO selectivity over 100 h on stream. The formation of carbide phases appears central to the suppression of CH_4 formation, underpinning the unique selectivity of these systems.

Beyond catalyst performance improvements, this work provides several key scientific contributions. First, it establishes a rationally engineered 2D/3D MoS_2@Ni/SBA-15 heterostructure capable of fully suppressing Ni-driven methanation through electronic modification. Second, it demonstrates that Mo oxide and Mo sulfide precursors, despite their different chemistries, dynamically converge into β-Mo_2C under RWGS conditions but at different phase transformation temperatures, providing direct evidence of reaction-induced carburisation. Third, the study identifies the emergence of Ni-Mo mixed carbides domains formed during high-temperature operation, explaining the loss of classical Ni methanation behaviour and the switch toward exclusive CO formation. Finally, the work validates an *in situ* activation strategy in which the active carbide phase forms under reaction conditions, avoiding the typical instability and reoxidation issues associated with pre-activated Mo_2C catalysts.

Experimental section

Chemicals

All chemicals needed for the preparation of SBA-15 and 2D/3D MoS_2@Ni/SBA-15 were used with no further purification: Pluronic P123 (Sigma Aldrich), hydrochloric acid (HCl, 37%, Sigma Aldrich), tetraethyl orthosilicate (TEOS, Sigma Aldrich), hexaammonium heptamolybdate tetrahydrate ($(NH_4)_6Mo_7O_{24}{\cdot}4H_2O$, Sigma Aldrich), and nickel(II) nitrate hexahydrate ($Ni(NO_3)_2{\cdot}6H_2O$, Fisher scientific).

Catalyst preparation

Synthesis of mesoporous SBA-15. The preparation of SBA-15 was performed under acidic conditions.[86] Initially, 47 g of Pluronic P123 was dissolved in a mixture of 233 mL of 37% hydrochloric acid and 1.5 L of deionized water in a 3 L glass reactor, followed by stirring at 40 °C for 24 h. After complete dissolution of P123, 112 mL of tetraethyl orthosilicate (TEOS) was added dropwise, and the resulting mixture was stirred for an additional 24 h at 40 °C. The solution was then heated to 100 °C and maintained at this temperature for 48 h to allow ageing. After cooling to room temperature, the solid product was recovered by filtration, washed thoroughly with deionized water until a neutral pH was reached, and subsequently dried at 60 °C. Finally, calcination was carried out at 550 °C for 6 h with a heating rate of 1.5 °C min^{-1}.

Synthesis of MoO_3@NiO/SBA-15. The MoO_3@NiO/SBA-15 oxide precursor was prepared by impregnation with aqueous solutions of ammonium heptamolybdate tetrahydrate ($(NH_4)_6Mo_7O_{24}{\cdot}4H_2O$) and nickel nitrate hexahydrate ($Ni(NO_3)_2{\cdot}6H_2O$) using a two-step incipient wetness method. After each impregnation step, the sample was dried at 60 °C for 12 h and calcined at 500 °C for 4 hours with heating rate of 3 °C min^{-1}. All of the obtained catalysts were pelletized and sieved into 200–300 μm particles. The metal compositions of the catalyst were 5 wt% Ni and 10 wt% Mo.

Synthesis of 2D/3D MoS_2@Ni/SBA-15. The 2D/3D MoS_2@Ni/SBA-15 heterostructure was synthesised *via in situ* gas-phase sulfidation of a MoO_3@NiO/SBA-15 oxidic support. In a typical synthesis, ~1 g of oxidic precursor (200–300 μm) were loaded in a quartz reactor and heated up to 400 °C with a 6 °C min^{-1} ramp rate in H_2S/H_2 (10% v/v) at a flow rate of 100 mL min^{-1}. The sample was kept under these conditions for 2 h and subsequently cooled to room temperature. The sulfided catalyst was then transferred to an Ar-filled glovebox for further testing and characterization.

Catalyst characterization

Transmission electron microscopy (TEM). The average particle size, size distribution, and morphology of both as-prepared and post-reaction catalysts were determined on a TITAN Themis 3007 S/TEM operated at an acceleration voltage of 300 kV. The microscope is equipped with multiple annular dark-field detectors and a Super-X detection system comprising four windowless silicon drift detectors for energy-dispersive X-ray spectroscopy (EDS). The microscope was operated with probe semi-convergence of 20 mrad resulting in probe size of about 0.5 nm and beam current of about 50 pA. High-angle annular dark-field (HAADF) imaging was performed with collection angles ranging from 50 to 200 mrad. EDS elemental mapping was carried out in spectrum imaging mode, employing a dwell time of 15 μs per pixel and continuous frame scanning for a total acquisition time of 20 minutes. For sample preparation, the catalysts were embedded in a polymeric resin, sectioned into 50 nm-thick slices using an ultramicrotome. Samples are subsequently placed on 200-mesh lacey carbon grids for analysis.

X-ray diffraction (XRD). Analysis was conducted on both as-prepared and post-reaction catalysts using a Bruker AXS D8 Advance diffractometer configured in Bragg–Brentano geometry and equipped with a LynxEye Super Speed detector. Patterns were collected using Cu Kα radiation (λ = 0.154 nm, 40 kV, 30 mA) over a 2θ range of 5–80° with a step size of 0.02° and a scan time of 0.5 s per step. Crystal phase identification was performed by comparison with the International Centre for Diffraction Data (ICDD) database. For air-sensitive 2D/3D MoS_2@Ni/SBA-15 and post-reaction catalysts, the materials were handled exclusively under inert atmosphere. The samples were kept sealed in the reaction tube using closed valves and transferred directly into a glove box filled with Ar. Inside the glove box, the samples were carefully extracted and placed onto a quartz holder, which was then covered with Kapton film to prevent exposure to air during analysis.

Low angle XRD. Measurements were performed on a Xeuss 2.0 system (Xenocs) operating under vacuum conditions,

equipped with a GeniX3D Cu microsource (λ = 1.5418 Å, 50 kV, 0.6 mA) and a Pilatus 3R 200K 2D detector. This allowed characterization of the mesostructural ordering and pore periodicity of the SBA-15 support before and after catalyst synthesis.

Nitrogen physisorption. The textural properties of the as-prepared catalysts were characterized by nitrogen physisorption at −196 °C using a Micromeritics TriStar II automated gas adsorption system equipped with MicroActive software (version 4.06). Prior to analysis, the samples were degassed under dynamic vacuum at 300 °C for 3 h to remove adsorbed moisture and volatiles. The specific surface area was calculated using the multipoint Brunauer–Emmett–Teller (BET) method, while the pore size distribution was determined from the desorption branch of the isotherm using the Barrett–Joyner–Halenda (BJH) model. The total pore volume (V_{pore}) was determined at a relative pressure (P/P_0) of 0.97, and the micropore volume (V_{micro}) was evaluated using the t-plot method.

Temperature-programmed reduction (H_2-TPR). H_2-TPR experiments were carried out on a Micromeritics AutoChem II chemisorption analyzer equipped with a thermal conductivity detector (TCD) for hydrogen quantification. Approximately 100 mg of catalyst was loaded into a quartz U-tube reactor, positioned between two plugs of quartz wool. Prior to reduction, the samples were purged under an argon flow to remove any adsorbed species. Then, the reduction was performed under a flow of 5 vol% H_2 in argon (50 mL min^{-1}), with the temperature ramped from 30 °C to 1000 °C at a heating rate of 10 °C min^{-1}. The hydrogen consumption was monitored continuously using a TCD, and the total H_2 uptake was determined by integrating the area under the TPR profiles within defined temperature ranges.

X-ray photoelectron spectroscopy (XPS). The surface chemical composition and oxidation states of the as-prepared and spent catalysts were analysed using a Kratos Analytical AXIS Ultra DLD spectrometer equipped with a monochromatic Al Kα X-ray source (1486.6 eV) and an electron analyzer operating at a fixed pass energy of 20 eV. For spent catalysts, samples were first treated under the reaction gas mixture ($H_2/CO_2/Ar$ = 50 : 12.5 : 37.5 mL min^{-1}) across a temperature range of 200–800 °C. After reaction, the system was cooled to room temperature, sealed, and transferred into an inert gas glovebox to prevent air exposure during storage and sample preparation. Samples were mounted on double-sided conductive carbon tape inside the glovebox and then directly transferred into the XPS chamber using a pre-treatment environmental activation chamber to maintain their surface states. Binding energies (BEs) were calibrated relative to the C 1s core level of adventitious carbon at 284.8 eV. Spectra fitting and decomposition were performed using CasaXPS software (version 2.3.24).

Laser Raman spectroscopy (LRS). Laser Raman spectroscopy (LRS) measurements were conducted at room temperature using a HORIBA XPLORA PLUS Raman microscope equipped with a 532 nm excitation laser. To avoid potential thermal damage caused by heating under the laser beam, a low laser power was imposed through the use of a density filter (1% of maximum power) throughout the analysis for the sulfided sample. Each spectral range was collected with three accumulations to improve signal-to-noise ratio. The Raman spectra were recorded in the range of 100–1100 cm^{-1}. No evidence of sample degradation under these conditions was observed. Data acquisition and post-processing were performed using the LABSPEC software.

Inductively coupled plasma optical emission spectroscopy (ICP-OES). Mo and Ni loadings of the as-prepared catalysts were determined by inductively coupled plasma optical emission spectrometry (ICP-OES) on an Agilent 5110 Vertical Dual View ICP-OES equipped with a OneNeb nebulizer instrument. Prior to analysis, approximately 30–40 mg of catalyst samples was subjected to a two-step wet acid digestion process at 120 °C to ensure complete dissolution. In the first step, the samples were treated with a mixture of hydrofluoric acid (HF) and nitric acid (HNO_3) for 24 hours, followed by a dry evaporation. The resulting residue was then redissolved in aqua regia (a mixture of HCl and HNO_3) and left for an additional 24 hours. After partial evaporation, the solutions were diluted to a final volume of 10 mL using ultrapure water.

CHNS analysis. The as-prepared and post-reaction catalysts were analysed for carbon, hydrogen, nitrogen and sulfur by using CHNS elemental analyser, with sulfanilic acid used as standard.

Activity measurements

The CO_2 hydrogenation experiments were conducted in a fixed-bed quartz microreactor. Granulated catalysts (200–300 μm particle size) were accurately weighed and loaded into the isothermal zone of the reactor. Prior to reaction, the catalyst underwent *in situ* reduction under a flow of 50% H_2/Ar (100 mL min^{-1}) at 600 °C for 1.5 hour, followed by cooling to 100 °C. Subsequently, a gas mixture containing 1 vol% CO_2 and 4 vol% H_2 (balanced with Ar) was introduced at a total flow rate of 100 mL min^{-1} under atmospheric pressure, resulting in a weight hourly space velocity (WHSV) of 12 000 mL g_{cat}^{-1} h^{-1}. The catalytic activity of 2D/3D MoS_2@Ni/SBA-15 was evaluated through two consecutive temperature-programmed reaction cycles performed from 200 °C to 800 °C, to assess both the activity and thermal stability of the catalyst under standard RWGS conditions. The outlet gas composition was continuously monitored using an online infrared gas analyser (XSTREAM XEGP-IR, EMERSON). Prior to IR detection, water was condensed out of the gas stream. The only carbon-containing products detected were CO, CH_4, and unconverted CO_2. CO_2 conversion ($X(CO_2)$), product selectivity (S), and product yield (r) were calculated using standard formulas.

$$X(CO_2) = \frac{F(CO_2)\text{in} - F(CO_2)\text{out}}{F(CO_2)\text{in}} \times 100$$

$$S(\text{product}) = \frac{F(\text{product})\text{out}}{F(CH_4)\text{out} + F(CO)\text{out}} \times 100$$

$$r(\text{product}) = X(CO_2) \times S(\text{product}) \times 100$$

Author contributions

Oumayma Liaaychi: conceptualization, formal analysis, investigation, methodology, visualization, writing – original draft. Pascal Blanchard: formal analysis, writing – review & editing. Maya Marinova: formal analysis, writing – review & editing; Carole Lamonier: writing – review & editing; Jean-Philippe Dacquin: supervision, formal analysis, writing – review & editing, funding acquisition. Sébastien Royer: supervision, formal analysis, writing – review & editing, funding acquisition; Said Laassiri: supervision, formal analysis, writing – review & editing, funding acquisition.

Conflicts of interest

The authors declare that they have no competing financial interests or personal relationships that could have influenced the work reported in this manuscript.

Data availability

All the data generated in this study are included in the article and its supplementary information (SI). Supplementary information is available. See DOI: https://doi.org/10.1039/d5ey00328h.

Acknowledgements

The authors gratefully acknowledge financial support from the Ministry of Europe and Foreign Affairs (MEAE), the Ministry of Higher Education and Research (MESR), and the Ministry of Higher Education, Scientific Research and Innovation (MESRSI) under the framework of the Franco-Moroccan bilateral PHC TOUBKAL 2023 program (Grant No. 12345AB AmmoniaLoop Toubkal/23/170-48539XJ). Funding and PhD support from Mohammed VI Polytechnic University (UM6P) are also gratefully acknowledged.

References

1 H. Zhang, *ACS Nano*, 2015, **9**, 9451–9469.
2 M. Zhang, Z. Wang, X. Bo, R. Huang and D. Deng, *Angew. Chem., Int. Ed.*, 2024, **64**, e202419661.
3 Y. S. Cho and J. Kang, *Nanoscale*, 2024, **16**, 3936–3950.
4 Y. Zhang, L. Li, S. X. Guo, X. Zhang, F. Li, A. M. Bond and J. Zhang, *ChemSusChem*, 2020, **13**, 59–77.
5 R. V. Mom, J. N. Louwen, J. W. M. Frenken and I. M. N. Groot, *Nat. Commun.*, 2019, **10**, 1–8.
6 A. Sfeir, C. E. Shuck, A. Fadel, M. Marinova, H. Vezin, J. P. Dacquin, Y. Gogotsi, S. Royer and S. Laassiri, *J. Am. Chem. Soc.*, 2024, **146**, 20033–20044.
7 L. Dong, J. Yang, X. Yue, S. Dong, W. Li and X. Li, *ACS Appl. Nano Mater.*, 2023, **6**, 18858–18868.
8 C. Álvarez Galván, J. Schumann, M. Behrens, J. L. G. Fierro, R. Schlögl and E. Frei, *Appl. Catal., B*, 2016, **195**, 104–111.
9 K. J. Lee, Y. Ye, H. Su, B. S. Mun and E. J. Crumlin, *ACS Catal.*, 2023, **13**, 9041–9050.
10 A. M. Bahmanpour, F. Héroguel, M. Kllç, C. J. Baranowski, L. Artiglia, U. Röthlisberger, J. S. Luterbacher and O. Kröcher, *ACS Catal.*, 2019, **9**, 6243–6251.
11 Z. Zhang, Y. Shu, Q. Liu, S. Bi and P. Zhang, *Chem. Eng. J.*, 2023, **475**, 146333.
12 M. V. Twigg and M. S. Spencer, *Appl. Catal., A*, 2001, **212**, 161–174.
13 K. N. Tamakuwala, R. P. Kennedy, C. S. Li, B. Mutz, P. Boller, S. R. Bare and M. W. Kanan, *JACS Au*, 2025, **5**, 1083–1089.
14 M. Sadeghnezhad, A. Bazyari, M. Rezaei and E. Akbari, *Int. J. Hydrogen Energy*, 2025, **151**, 150093.
15 J. H. Kwak, L. Kovarik and J. Szanyi, *ACS Catal.*, 2013, **3**, 2449–2455.
16 J. Dou, Y. Sheng, C. Choong, L. Chen and H. C. Zeng, *Appl. Catal., B*, 2017, **219**, 580–591.
17 A. García-Zaragoza, J. L. del Río-Rodríguez, C. Cerezo-Navarrete, S. Gutiérrez-Tarriño, M. A. Molina, L. Costley-Wood, J. Mazarío, B. Chaudret, L. M. Martínez-Prieto, A. M. Beale and P. Oña-Burgos, *ACS Catal.*, 2025, **15**, 9489–9502.
18 M. Rajput, S. K. Mallik, S. Chatterjee, A. Shukla, S. Hwang, S. Sahoo, G. V. P. Kumar and A. Rahman, *Commun. Mater.*, 2024, **5**, 1–14.
19 M. Kashif, S. Thangarasu and T. H. Oh, *Int. J. Hydrogen Energy*, 2024, **82**, 47–52.
20 I. H. Sajid, M. Z. Iqbal and S. Rizwan, *RSC Adv.*, 2024, **14**, 6823–6847.
21 C. Han, Z. Tian, H. Dou, X. Wang and X. Yang, *Chin. Chem. Lett.*, 2018, **29**, 606–611.
22 E. Pomerantseva and Y. Gogotsi, *Nat. Energy*, 2017, **2**, 17089.
23 C. Yang, W. Wang, D. Wang, M. Gong, Y. Xin, L. Xiao, O. V. Kikhtyanin, D. Kubicka and W. Wu, *J. Environ. Chem. Eng.*, 2022, **10**, 107761.
24 J. Zhou, W. An, Z. Wang and X. Jia, *Catal. Sci. Technol.*, 2019, **9**, 4314–4326.
25 A. Ungureanu, B. Dragoi, A. Chirieac, S. Royer, D. Duprez and E. Dumitriu, *J. Mater. Chem.*, 2011, **21**, 12529–12541.
26 J. Wang, H. Zhou, J. Zhuang and Q. Liu, *Sci. Rep.*, 2013, **3**, 1–7.
27 K. B. Baharudin, Y. H. Taufiq-Yap, J. Hunns, M. Isaacs, K. Wilson and D. Derawi, *Microporous Mesoporous Mater.*, 2019, **276**, 13–22.
28 B. Li, L. Jiang, X. Li, P. Ran, P. Zuo, A. Wang, L. Qu, Y. Zhao, Z. Cheng and Y. Lu, *Sci. Rep.*, 2017, **7**, 1–12.
29 G. Hu, W. Li, J. Xu, G. He, Y. Ge, Y. Pan, J. Wang and B. Yao, *Mater. Lett.*, 2016, **170**, 179–182.
30 X. K. Hu, Y. T. Qian, Z. T. Song, J. R. Huang, R. Cao and J. Q. Xiao, *Chem. Mater.*, 2008, **4**, 1527–1533.
31 K. Eda, *J. Solid State Chem.*, 1992, **98**, 350–357.
32 R. Ionescu, B. Campbell, R. Wu, E. Aytan, A. Patalano, I. Ruiz, S. W. Howell, A. E. McDonald, T. E. Beechem, K. A. Mkhoyan, M. Ozkan and C. S. Ozkan, *Sci. Rep.*, 2017, **7**, 6419.

33 R. Luo, W. W. Xu, Y. Zhang, Z. Wang, X. Wang, Y. Gao, P. Liu and M. Chen, *Nat. Commun.*, 2020, **11**, 1011.
34 E. Hu, Z. Yao, L. Zhao, J. Wu, H. Meng, L. Huo and Y. Li, *Can. J. Chem. Eng.*, 2019, **97**, 1107–1113.
35 Z. Zhang, Q. Wang and X. Zhang, *Catalysts*, 2019, **9**, 466.
36 X. Zhou, J. Liu, L. Zhang, S. Wang, X. Jia, W. Fu and T. Tang, *Appl. Organomet. Chem.*, 2023, **37**, e7080.
37 G. B. McGarvey and S. Kasztelan, *J. Catal.*, 1994, **148**, 149–156.
38 X. S. Li, Q. Xin, X. X. Guo, P. Grange and B. Delmon, *J. Catal.*, 1992, **137**, 385–393.
39 P. Kalita, P. J. Boruah, A. R. Pal and H. Bailung, *Dalton Trans.*, 2024, **53**, 11071–11087.
40 W. Tong, Y. Wang, Y. Bian, A. Wang, N. Han and Y. Chen, *Nanoscale Res. Lett.*, 2020, **15**, 35.
41 A. A. Bessonov, M. N. Kirikova, D. I. Petukhov, M. Allen, T. Ryhänen and M. J. A. Bailey, *Nat. Mater.*, 2015, **14**, 199–204.
42 C. Jung, H. I. Yang and W. Choi, *Nanoscale Res. Lett.*, 2019, **14**, 1–8.
43 M. A. Baker, R. Gilmore, C. Lenardi and W. Gissler, *Appl. Surf. Sci.*, 1999, **150**, 255–262.
44 X. Fan, B. Li, C. Zhu, F. Yan, X. Zhang and Y. Chen, *Small*, 2024, **20**, 2309655.
45 Z. Zhang, Y. Zang, F. Gao, J. Qu, J. Gu and X. Lin, *New J. Chem.*, 2022, **46**, 22332–22340.
46 Q. Zhang, M. Bown, L. Pastor-Pérez, M. S. Duyar and T. R. Reina, *Ind. Eng. Chem. Res.*, 2022, **61**, 12857–12865.
47 Y. Zhuang, R. Currie, K. B. McAuley and D. S. A. Simakov, *Appl. Catal., B*, 2019, **575**, 74–86.
48 A. R. Querido, L. P. L. Gonçalves, Y. V. Kolen'ko, M. F. R. Pereira and O. S. G. P. Soares, *Catal. Sci. Technol.*, 2023, **13**, 3606–3613.
49 W. Gac, W. Zawadzki, M. Rotko, G. Słowik and M. Greluk, *Top. Catal.*, 2019, **62**, 524–534.
50 M. Tommasi, A. Gramegna, A. Di Michele, E. Falletta, F. Galli, L. Prati, C. Hammond and I. Rossetti, *Int. J. Hydrogen Energy*, 2025, **136**, 948–965.
51 Y. Liu and D. Liu, *Int. J. Hydrogen Energy*, 1999, **24**, 351–354.
52 X. Zhang, X. Zhu, L. Lin, S. Yao, M. Zhang, X. Liu, X. Wang, Y. W. Li, C. Shi and D. Ma, *ACS Catal.*, 2016, **7**, 912–918.
53 A. Okemoto, M. R. Harada, T. Ishizaka, N. Hiyoshi and K. Sato, *Appl. Catal., B*, 2020, **592**, 117415.
54 L. Yang, L. Pastor-Pérez, S. Gu, A. Sepúlveda-Escribano and T. R. Reina, *Appl. Catal., B*, 2018, **232**, 464–471.
55 E. Gioria, P. Ingale, F. Pohl, R. Naumann d'Alnoncourt, A. Thomas and F. Rosowski, *Catal. Sci. Technol.*, 2022, **12**, 474–487.
56 X. Yang, X. Su, X. Chen, H. Duan, B. Liang, Q. Liu, X. Liu, Y. Ren, Y. Huang and T. Zhang, *Appl. Catal., B*, 2017, **216**, 95–105.
57 B. Liang, H. Duan, X. Su, X. Chen, Y. Huang, X. Chen, J. J. Delgado and T. Zhang, *Catal. Today*, 2017, **281**, 319–326.
58 X. Zhang, S. Han, B. Zhu, G. Zhang, X. Li, Y. Gao, Z. Wu, B. Yang, Y. Liu, W. Baaziz, O. Ersen, M. Gu, J. T. Miller and W. Liu, *Nat. Catal.*, 2020, **3**, 411–417.
59 H. C. Wu, Y. C. Chang, J. H. Wu, J. H. Lin, I. K. Lin and C. S. Chen, *Catal. Sci. Technol.*, 2015, **5**, 4154–4163.
60 A. Ranjbar, A. Irankhah and S. F. Aghamiri, *J. Environ. Chem. Eng.*, 2018, **6**, 4945–4952.
61 L. R. Winter, R. Chen, X. Chen, K. Chang, Z. Liu, S. D. Senanayake, A. M. Ebrahim and J. G. Chen, *Appl. Catal., B*, 2019, **245**, 360–366.
62 Z. Zhang, Y. Tian, L. Zhang, S. Hu, J. Xiang, Y. Wang, L. Xu, Q. Liu, S. Zhang and X. Hu, *Int. J. Hydrogen Energy*, 2019, **44**, 9291–9306.
63 K. F. Kalz, R. Kraehnert, M. Dvoyashkin, R. Dittmeyer, R. Gläser, U. Krewer, K. Reuter and J. D. Grunwaldt, *ChemCatChem*, 2017, **9**, 17–29.
64 Z. Zhang, B. Zandkarimi and A. N. Alexandrova, *Acc. Chem. Res.*, 2020, **53**, 447–458.
65 X. Sun, J. Yu, H. Zada, Y. Han, L. Zhang, H. Chen, W. Yin and J. Sun, *Nat. Chem.*, 2024, **16**, 2044–2053.
66 H. Xin, R. Li, L. Lin, R. Mu, M. Li, D. Li, Q. Fu and X. Bao, *Nat. Commun.*, 2024, **15**, 1–8.
67 J. Ni, Z. Ruan, S. Zhu, X. Kan, L. Lu and Y. Liu, *ChemElectroChem*, 2019, **6**, 5958–5966.
68 G. Sun, Q. Zhao, T. Wu, W. Lu, M. Bao, L. Sun, H. Xie and J. Liu, *ACS Appl. Mater. Interfaces*, 2018, **10**, 6327–6335.
69 J. Zhang, T. Wang, C. Shi, L. Pan, X. Zhang, C. Peng and J. J. Zou, *Chem. Eng. J.*, 2023, **470**, 144197.
70 X. Du, R. Li, H. Xin, Y. Fan, C. Liu, X. Feng, J. Wang, C. Dong, C. Wang, D. Li, Q. Fu and X. Bao, *Angew. Chem., Int. Ed.*, 2024, **63**, e202411761.
71 J. Jeon, Y. Park, S. Choi, J. Lee, S. S. Lim, B. H. Lee, Y. J. Song, J. H. Cho, Y. H. Jang and S. Lee, *ACS Nano*, 2018, **12**, 338–346.
72 M. Chufarov, Y. Z. Vassilyeva, X. Zhang, S. Li, A. Y. Pak and W. Han, *iScience*, 2024, **27**, 110551.
73 L. Jiang, R. Wang, H. Zhou, G.-F. Wei and X. Wang, *J. Mater. Chem. A*, 2024, **12**, 3557–3564.
74 H. Wang, X. Qin, Z. Gao, Y. Diao, S. Liu, M. Peng, S. Liu, S. Hou, X. Liu, X. Guo, D. Ma and C. Shi, *Nat. Commun.*, 2025, **16**, 11383.
75 Y. Diao, X. Zhang, Y. Liu, B. Chen, G. Wu and C. Shi, *Appl. Catal., B*, 2022, **301**, 120779.
76 H. Zhou, Z. Chen, E. Kountoupi, A. Tsoukalou, P. M. Abdala, P. Florian, A. Fedorov and C. R. Müller, *Nat. Commun.*, 2021, **12**, 1–10.
77 C. Shi, A. Zhang, X. Li, S. Zhang, A. Zhu, Y. Ma and C. Au, *Appl. Catal., A*, 2012, **431–432**, 164–170.
78 T. S. Galhardo, A. H. Braga, B. H. Arpini, J. Szanyi, R. V. Gonçalves, B. F. Zornio, C. R. Miranda and L. M. Rossi, *J. Am. Chem. Soc.*, 2021, **143**, 4268–4280.
79 T. Hyeon, M. Fang and K. S. Suslick, *J. Am. Chem. Soc.*, 1996, **118**, 5492–5493.
80 Y. Deng, Y. Ge, M. Xu, Q. Yu, D. Xiao, S. Yao and D. Ma, *Acc. Chem. Res.*, 2019, **52**, 3372–3383.
81 M. D. Porosoff, X. Yang, J. A. Boscoboinik and J. G. Chen, *Angew. Chem., Int. Ed.*, 2014, **53**, 6705–6709.

82 J. Gao, Y. Wu, C. Jia, Z. Zhong, F. Gao, Y. Yang and B. Liu, *Catal. Commun.*, 2016, **84**, 147–150.
83 L. R. Karadaghi, M. S. Madani, E. M. Williamson, A. T. To, S. E. Habas, F. G. Baddour, J. A. Schaidle, D. A. Ruddy, R. L. Brutchey and N. Malmstadt, *ACS Appl. Nano Mater.*, 2022, **5**, 1966–1975.
84 M. Ahmadi Khoshooei, G. Vitale, L. Carbognani and P. Pereira-Almao, *Catal. Sci. Technol.*, 2022, **12**, 6184–6194.
85 X. Du, R. Zhang, D. Li, C. Hu and H. Garcia, *J. Energy Chem.*, 2022, **73**, 68–87.
86 D. Zhao, J. Sun, Q. Li and G. D. Stucky, *Chem. Mater.*, 2000, **12**, 275–279.